

Electronic Supplementary Information

Effects of Water Vapor on the Reaction of CH₂OO with NH₃

Wen Chao,^a Cangtao Yin,^a Kaito Takahashi^a and Jim Jr-Min Lin,^{a,b*}

Table of Contents

Error Estimation	S2
Summary of the experimental conditions of CH ₂ OO+NH ₃ +H ₂ O reaction (Table S1)	S3
k_{obs} of CH ₂ OO as a function of [NH ₃] at fixed [H ₂ O] (Fig. S1–S10)	S5
Surface plot of k_{obs} (Fig. S11–S14)	S10
Summary of the kinetic results of CH ₂ OO+NH ₃ reaction (Fig. S15 and S16)	S12
Summary of the kinetic results of CH ₂ OO+2H ₂ O reaction (Fig. S17 and S18)	S13
Summary of the bimolecular rate coefficients and activation energies (Fig. S19)	S14
Details of quantum chemistry calculation	S15
Summary of the calculated energies and rate coefficients (Table S2)	S15
Key geometries for CH ₂ OO+NH ₃ , CH ₂ OO+2NH ₃ and CH ₂ OO+H ₂ O+NH ₃ (cat.) (Fig. S20)	S16
Energy profiles of NH ₃ and H ₂ O catalysis channels (Fig. S21)	S17
Rotational temperatures and vibrational frequencies of H-bonding complexes (Table S3)	S19
Summary of the equilibrium constants of H-bonding complexes (Table S4, Fig. S22)	S20
The calculated rate coefficients (Table S5)	S21
Representative temporal profiles for CH ₂ OO+NH ₃ +H ₂ O experiments (Fig. S23–S39)	S22
Cartesian coordinates of the calculated geometries (Table S6–S8)	S39
References	S44

Error Estimation

The termolecular reaction rate coefficient was derived from the slope of the effective rate coefficient, k_{eff} , as a function of the reactant concentrations. The main error may include contributions from the scattering of k_{eff} and the determining of the reactant concentrations. The reported error was derived by assuming each error is independent.

The concentration of NH_3 was determined by measuring its UV absorption signal within 200-250 nm and using Beer-Lambert law, $\text{Absorbance} = \ln(I_0/I) = \sigma L[\text{NH}_3]$. Here, I_0 and I are the transmitted light intensities without and with NH_3 , L is the length of the small absorption cell and σ is the reported absorption cross section of NH_3 . The small baseline drifting is further corrected by subtracting the absorbance change near 250 nm where NH_3 does not absorb. The error in $[\text{NH}_3]$, $\varepsilon_{[\text{NH}_3]}$, which mainly comes from the reported uncertainty in the cross section of NH_3 , is about 10%.¹

$[\text{H}_2\text{O}]$ was measured with a relative humidity (RH) sensor, whose accuracy is 0.8% of the full scale (100% RH). Thus the relative error is the ratio of 0.8% to the measured relative humidity. The typical relative humidity in the experiment is higher than 10% ($[\text{H}_2\text{O}] = 0.7 \times 10^{17} \text{ cm}^{-3}$), resulting in relative error of $0.8\%/10\% = 8\%$. Since the saturated water vapor pressure strongly depends on temperature (7% per Kelvin near room temperature) and the temperature stability of our reaction cell is about 0.5 K, the error caused by the temperature instability is $(7\% \text{ K}^{-1}) \times (0.5\text{K}) = 3.5\%$. Therefore, the total percentage error of $[\text{H}_2\text{O}]$ can be estimated to be $\varepsilon_{[\text{H}_2\text{O}]} = \sqrt{8\%^2 + 3.5\%^2} = 8.7\%$.

The $[\text{H}_2\text{O}]$ and $[\text{NH}_3]$ in the photolysis cell were calculated from the measured concentrations and the gas mixing ratios by assuming ideal gas behavior. The concentrations were measured separately to prevent interference from the other species. The calibrated temperature sensors (Rotronic humidity sensor or resistance temperature detector) and pressure sensors have relative error smaller than 1%. All the gas flows were controlled by mass flow controllers and the overall percentage error of gas mixing, ε_{mix} , was estimated to be 5% according to the accuracy levels claimed by instrument suppliers.

The scattering of k_{eff} is estimated by linear regression process to get the termolecular reaction rate coefficient. We used 1 standard deviation to present the error of scattering, ε_{fit} , which is about 2%. Therefore, the final error of the termolecular rate coefficient is estimated as $\varepsilon_k = \sqrt{10\%^2 + 8.7\%^2 + 5\%^2 + 2\%^2} = 14\%$. The errors of $\text{CH}_2\text{OO}+2\text{H}_2\text{O}$ and $\text{CH}_2\text{OO}+\text{NH}_3$ reactions are also estimated in a similar manner.

Finally, since the activation energy only depends on the relative change of the rate coefficient, we only used the error from the fitting of the Arrhenius equation as the error bar for the activation energy.

Table S1. Summary of the experimental conditions of CH₂OO reaction kinetics by scanning [NH₃] at fixed [H₂O].

Exp #	[H ₂ O] /10 ¹⁷ cm ⁻³	[CH ₂ I ₂] /10 ¹⁴ cm ⁻³	P _{total} /Torr	T /K	P _{O₂} /Torr	I _{248nm} /mJ cm ⁻²	[CH ₂ OO] ₀ /10 ¹¹ cm ⁻³	k ₀ /s ⁻¹	k _{eff} /10 ⁻¹⁴ cm ³ s ⁻¹
1	0.0	0.5	252.7	298.3	10.5	2.3	1.9*	43 ± 23 [†]	7.1 ± 0.2 [†]
2	1.5	0.5	252.9	298.4	10.6	2.3	1.9	274 ± 86	19.7 ± 0.5
3	2.7	0.5	252.9	298.4	10.5	2.3	1.8	1155 ± 317	27.2 ± 1.8
4	2.1	0.5	252.9	298.4	10.5	2.3	1.8	589 ± 95	23.7 ± 0.6
5	0.7	0.5	252.9	298.4	10.6	2.3	2.0	131 ± 51	12.4 ± 0.3
6	0.7	1.0	253.7	298.5	10.6	2.3	3.7	216 ± 28	11.8 ± 0.2
7	2.8	1.0	253.6	298.4	10.5	2.3	3.5	1371 ± 71	28 ± 0.4
8	0.0	1.0	253.8	298.4	10.6	2.3	3.9	121 ± 14	6.6 ± 0.1
9	1.5	1.0	253.8	298.4	10.6	2.3	3.7	448 ± 120	18.2 ± 0.7
10	2.1	1.0	253.8	298.4	10.5	2.3	3.6	663 ± 124	23.5 ± 0.8
11	0.0	0.2	101.0	298.4	4.2	2.3	2.3	70 ± 12	6.7 ± 0.1
12	0.6	0.2	101.0	298.4	4.2	2.3	2.2	155 ± 74	10.9 ± 0.6
13	1.0	0.2	101.1	298.4	4.2	2.3	2.3	177 ± 78	13.8 ± 0.5
14	1.5	0.2	101.0	298.4	4.2	2.3	2.1	325 ± 30	17.7 ± 0.2
15	2.1	0.2	101.1	298.4	4.2	2.3	2.2	678 ± 67	22.8 ± 0.6
16	0.0	1.1	251.8	278.0	10.2	2.3	3.8	130 ± 23	7.3 ± 0.1
17	0.4	1.2	251.7	278.0	10.2	2.3	3.8	243 ± 59	17.2 ± 0.3
18	0.9	1.2	251.7	278.0	10.2	2.3	3.8	610 ± 102	26.2 ± 0.6
19	1.2	1.2	251.7	278.0	10.2	2.3	3.8	1101 ± 145	33.8 ± 0.8
20	1.7	1.2	251.8	278.0	10.2	2.3	3.8	1999 ± 332	41.8 ± 1.9
21	0.0	1.1	251.6	288.1	10.2	2.3	4.2	147 ± 22	6.6 ± 0.1
22	0.9	1.1	251.6	288.1	10.2	2.3	4.1	402 ± 34	18.9 ± 0.2
23	1.9	1.1	251.7	288.1	10.2	2.3	3.9	1009 ± 88	31.3 ± 0.5
24	2.8	1.1	251.6	288.1	10.2	2.3	3.9	2311 ± 222	45.5 ± 1.3
25	3.7	1.1	251.6	288.1	10.2	2.3	3.6	4352 ± 333	57.9 ± 1.9
26	0.0	1.1	252.1	298.3	10.2	2.3	4.4	140 ± 21	6.7 ± 0.1
27	2.8	1.1	252.1	298.3	10.2	2.3	4.0	1293 ± 72	28.1 ± 0.4
28	4.5	1.1	252.1	298.3	10.2	2.3	3.8	3277 ± 266	44.9 ± 1.6
29	6.0	1.1	252.1	298.3	10.1	2.3	3.6	6420 ± 80	56.4 ± 0.5
30	0.0	1.1	252.8	308.5	10.2	2.3	4.5	150 ± 26	6.7 ± 0.2
31	1.6	1.1	252.4	308.5	10.2	2.3	4.2	393 ± 44	14.5 ± 0.3
32	2.8	1.1	252.5	308.5	10.2	2.3	4.0	804 ± 38	20.1 ± 0.2

33	4.1	1.1	252.6	308.5	10.2	2.3	3.8	1668 ± 57	26 ± 0.4
34	6.0	1.1	252.8	308.5	10.1	2.3	3.7	3420 ± 172	35.7 ± 1.1
35	0.0	1.1	250.8	298.3	10.1	2.5	4.6	185 ± 20	6.5 ± 0.1
36	1.3	1.1	251.0	298.4	10.1	2.5	4.3	409 ± 38	17 ± 0.2
37	2.8	1.1	251.4	298.3	10.1	2.5	4.2	1303 ± 62	27.4 ± 0.4
38	4.2	1.1	250.9	298.3	10.1	2.5	4.2	2828 ± 166	42.3 ± 1.0
39	5.6	1.1	250.9	298.4	10.0	2.5	3.9	5704 ± 169	52.3 ± 1.0
40	0.0	7.4	766.9	298.3	31.0	2.5	5.7	321 ± 33	5.9 ± 0.1
41	1.7	7.7	766.2	298.3	32.1	2.5	5.8	618 ± 116	20.4 ± 0.4
42	3.1	7.5	766.4	298.3	31.0	2.5	5.4	1451 ± 219	35.2 ± 0.9
43	4.7	7.3	766.6	298.3	30.6	2.5	5.1	4254 ± 459	51.2 ± 1.9
44	6.4	7.4	767.0	298.3	30.5	2.5	4.9	9055 ± 338	70.4 ± 1.4
45	0.0	3.1	505.6	298.3	20.1	2.5	4.7	230 ± 22	6.1 ± 0.1
46	1.7	3.1	501.7	298.3	20.1	2.5	4.9	604 ± 60	20.2 ± 0.4
47	3.0	3.1	501.7	298.3	20.1	2.5	4.6	1501 ± 110	31.4 ± 0.7
48	4.6	3.1	501.7	298.3	20.1	2.5	4.4	3773 ± 180	46 ± 1.1
49	6.2	3.1	502.4	298.3	20.1	2.5	4.2	7832 ± 340	59.7 ± 2.0

* The initial concentrations were derived without adding NH₃ and H₂O ($\sigma_{340\text{nm}} = 1.22 \times 10^{-17} \text{ cm}^2$).²

[†] Only fitting error (± 1 standard deviation).

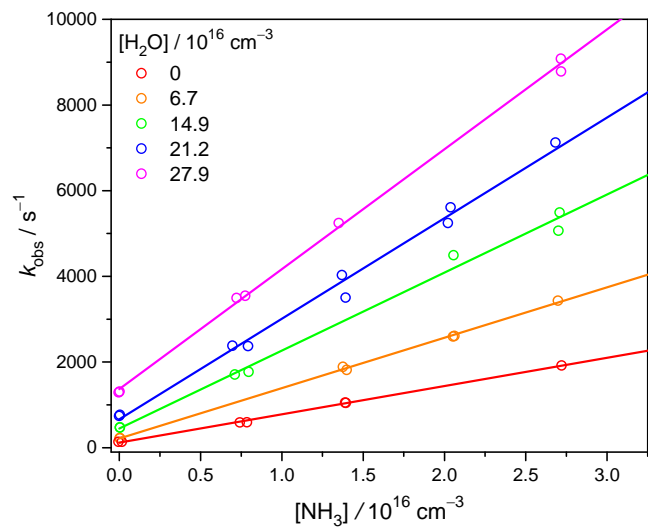


Figure S1. Plot of k_{obs} as a function of $[\text{NH}_3]$ under 298 K and 253 Torr (Exp# 1–5).

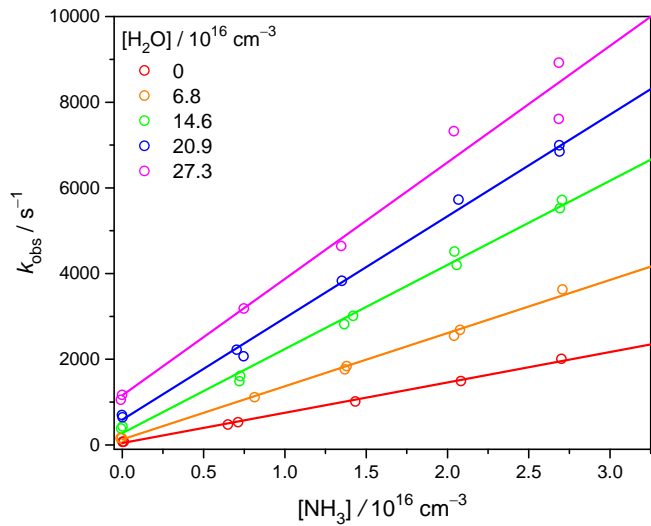


Figure S2. Plot of k_{obs} as a function of $[\text{NH}_3]$ under 298 K and 254 Torr (Exp# 6–10).

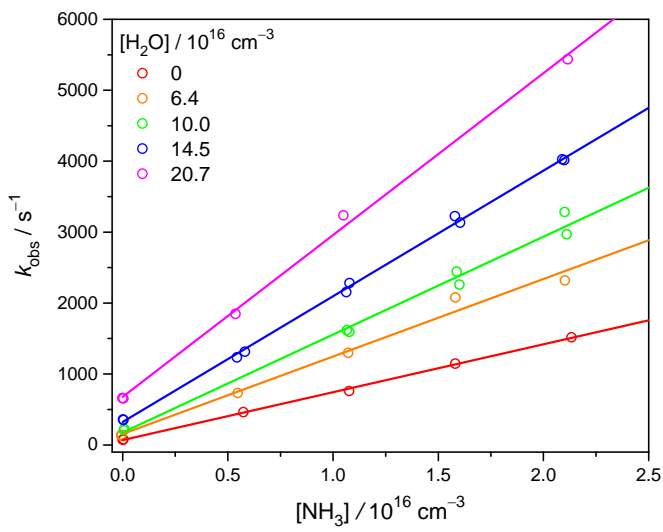


Figure S3. Plot of k_{obs} as a function of $[\text{NH}_3]$ under 298 K and 101 Torr (Exp#11–15).

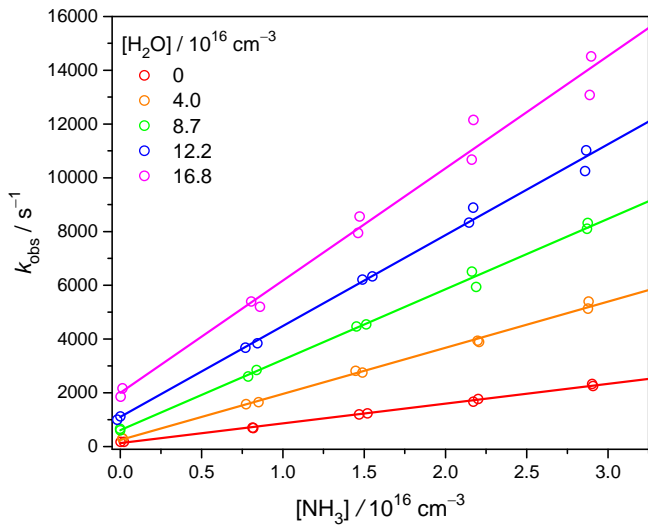


Figure S4. Plot of k_{obs} as a function of $[\text{NH}_3]$ under 278 K and 252 Torr (Exp#16–20).

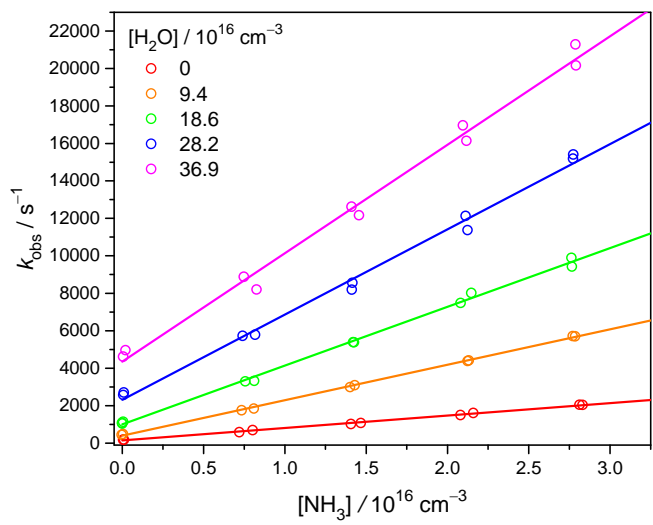


Figure S5. Plot of k_{obs} as a function of $[\text{NH}_3]$ under 288 K and 252 Torr (Exp#21–25).

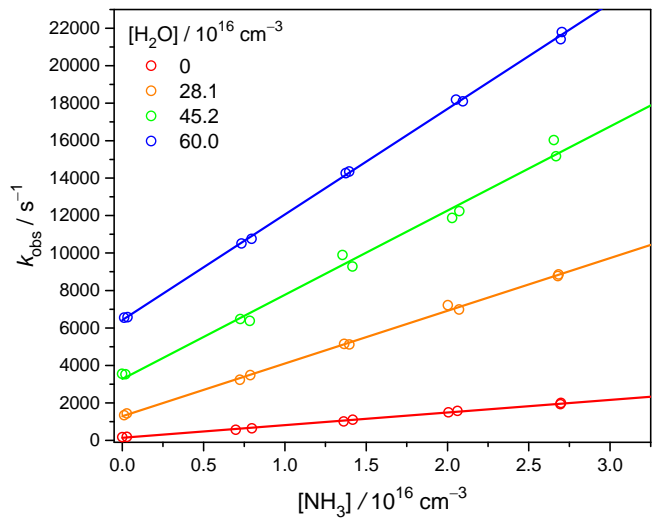


Figure S6. Plot of k_{obs} as a function of $[\text{NH}_3]$ under 298 K and 252 Torr (Exp#26–29).

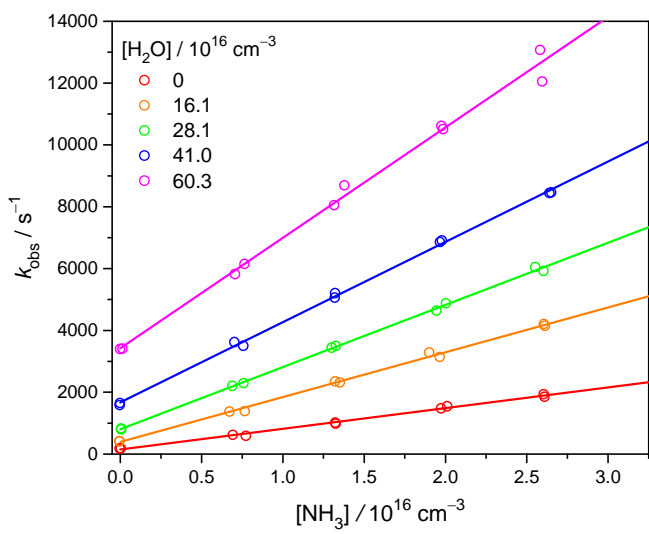


Figure S7. Plot of k_{obs} as a function of $[\text{NH}_3]$ under 308 K and 253 Torr (Exp#30–34).

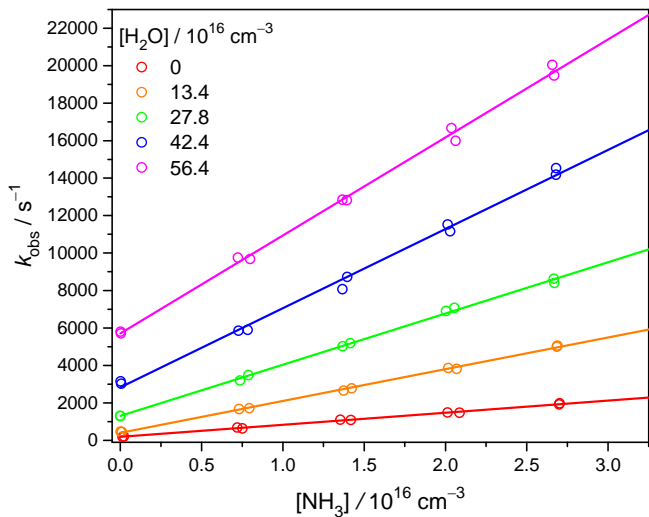


Figure S8. Plot of k_{obs} as a function of $[\text{NH}_3]$ under 298 K and 251 Torr (Exp#35–39).

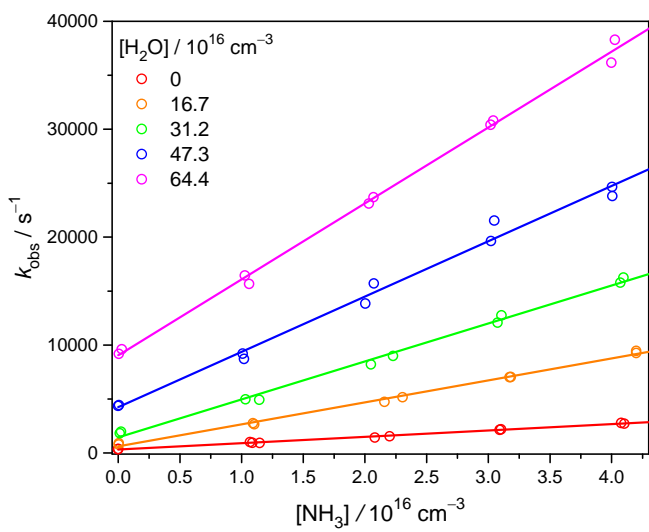


Figure S9. Plot of k_{obs} as a function of $[\text{NH}_3]$ under 298 K and 767 Torr (Exp#40–44).

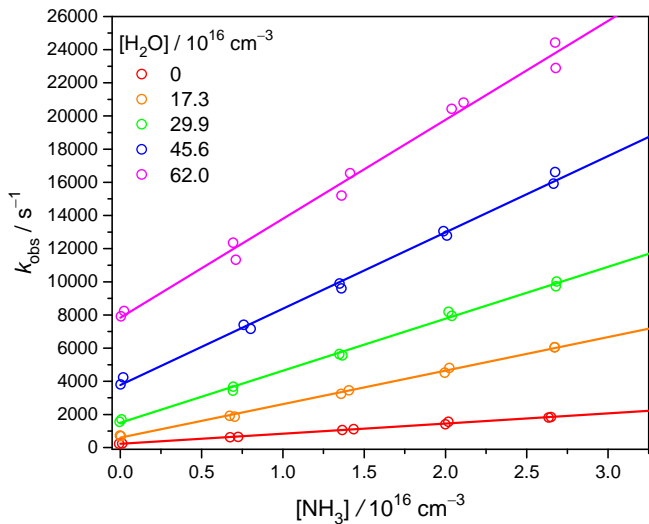


Figure S10. Plot of k_{obs} as a function of $[\text{NH}_3]$ under 298 K and 503 Torr (Exp#45–49).

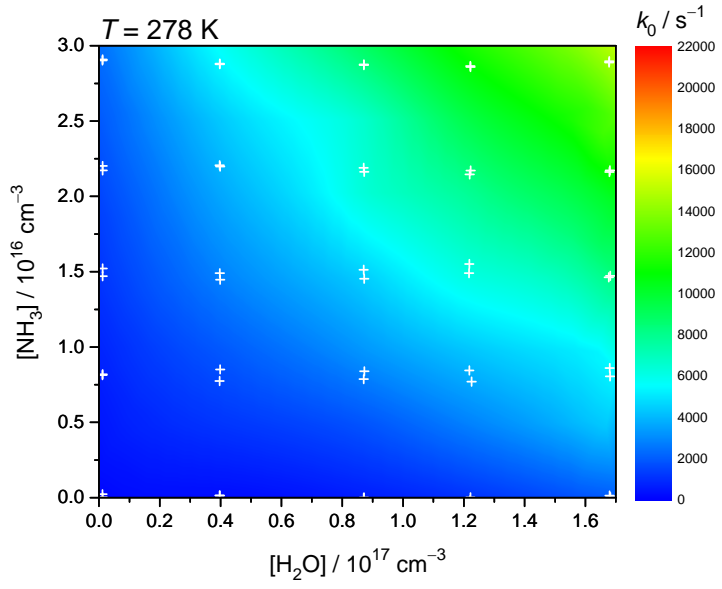


Figure S11. Surface plot of k_{obs} against $[\text{NH}_3]$ and $[\text{H}_2\text{O}]$ under 252 Torr and 278 K (Exp#16–20). White “+” symbols denote the experimental data that were used to construct the surface by using thin-plate-spline method (with Origin 9.1 graphing software).

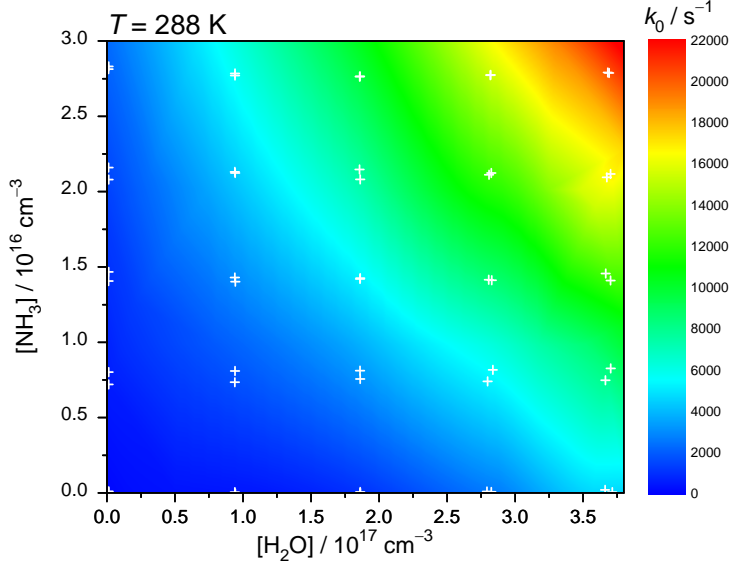


Figure S12. Surface plot of k_{obs} on both $[\text{NH}_3]$ and $[\text{H}_2\text{O}]$ under 252 Torr and 288 K (Exp#21–25). White “+” symbols denote the experimental data that were used to construct the surface by using thin-plate-spline method (with Origin 9.1 graphing software).

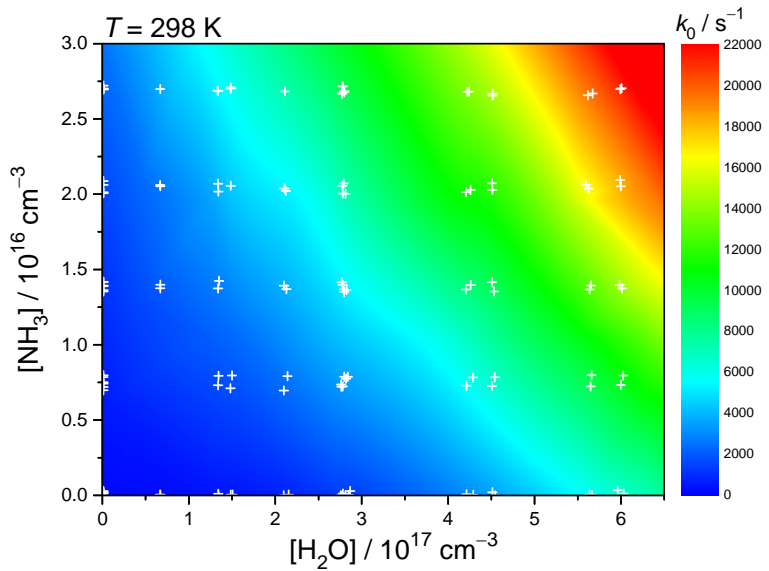


Figure S13. Surface plot of k_{obs} on both $[\text{NH}_3]$ and $[\text{H}_2\text{O}]$ under 252 Torr and 298 K (Exp#1–5, 26–29, and 35–39). White “+” symbols denote the experimental data that were used to construct the surface by using thin-plate-spline method (with Origin 9.1 graphing software).

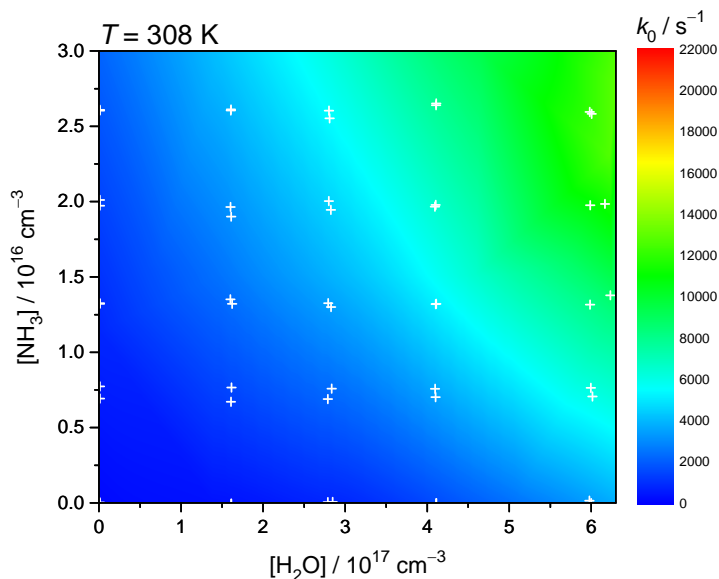


Figure S14. Surface plot of k_{obs} on both $[\text{NH}_3]$ and $[\text{H}_2\text{O}]$ under 253 Torr and 308 K (Exp#30–34). White “+” symbols denote the experimental data that were used to construct the surface by using thin-plate-spline method (with Origin 9.1 graphing software).

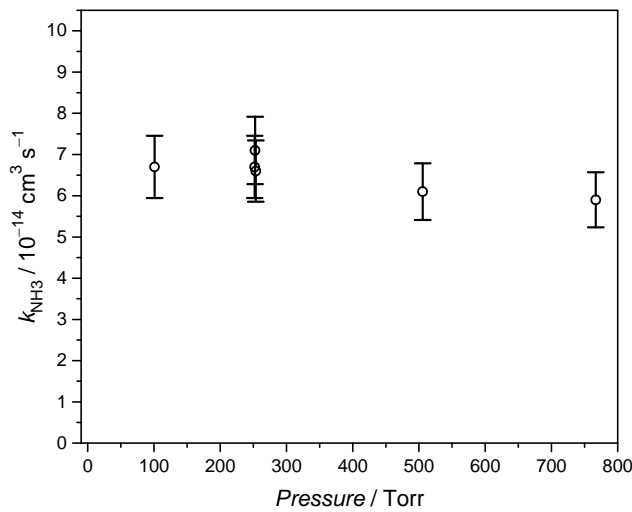


Figure S15. The pressure effect on the reaction rate coefficient of $\text{CH}_2\text{OO}+\text{NH}_3$ reaction.

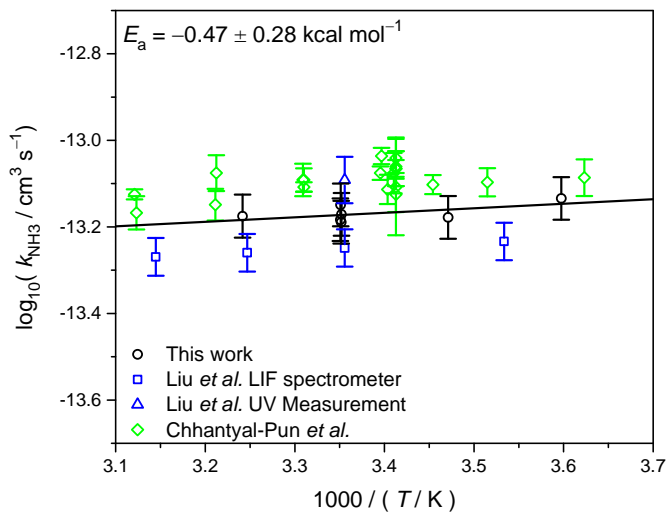


Figure S16. Arrhenius plot of the reaction rate coefficients of $\text{CH}_2\text{OO}+\text{NH}_3$. Solid line is linear regression to the data of this work (open black circles) (Exp# 1, 8, 16, 21, 26, 30, and 35). Experimental results of previous works (blue and green symbols)^{3,4} are also shown.

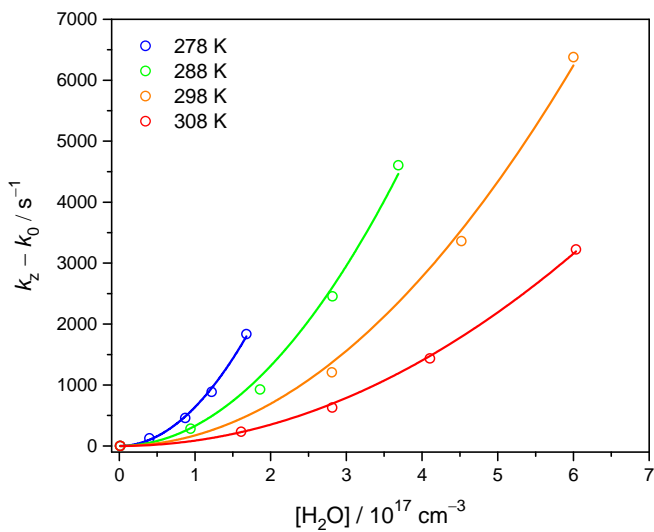


Figure S17. Plot of the decay rate coefficient at $[\text{NH}_3] = 0 \text{ cm}^{-3}$ (k_z), subtracted the background decay rate coefficient (k_0), as a function of $[\text{H}_2\text{O}]$ under different temperatures (Exp#16–34). The curves are pure quadratic fit.

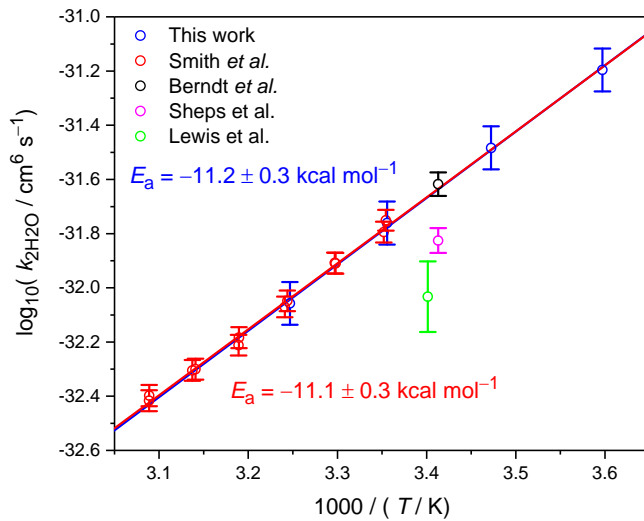


Figure S18. Arrhenius plot of the reaction coefficients of $\text{CH}_2\text{OO} + 2\text{H}_2\text{O}$ of this work (blue) and Smith *et al.* (red).⁵ The reported bimolecular rate coefficients of $\text{CH}_2\text{OO} + (\text{H}_2\text{O})_2$ reaction are converted into termolecular rate coefficients of $\text{CH}_2\text{OO} + 2\text{H}_2\text{O}$ reaction by considering the water dimerization constant for the previous works.^{5,6} Solid lines are linear regression. We further used the rate coefficient of $\text{CH}_2\text{OO} + \text{SO}_2$, $k = (3.6 \pm 0.4) \times 10^{-11} \text{ cm}^3 \text{ s}^{-1}$,⁷ to derived the corresponding rate coefficient of $\text{CH}_2\text{OO} + 2\text{H}_2\text{O}$ (black) from the reported relative rate coefficient of Berndt *et al.*⁶ The results of Sheps *et al.*⁸ (magenta) and Lewis *et al.*⁹ (green) are also included.

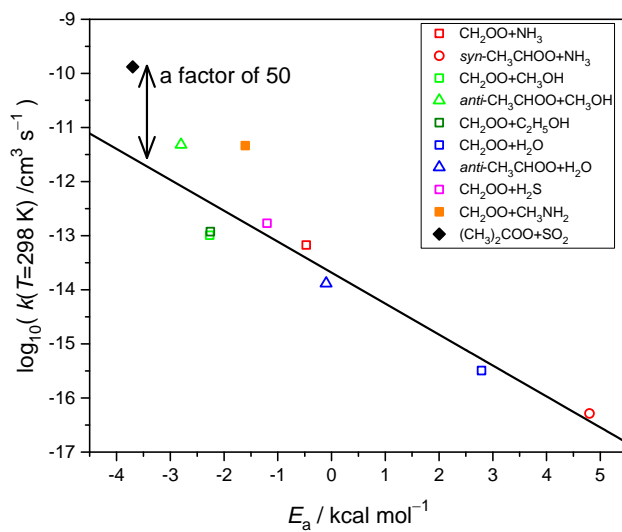


Figure S19. Plot of the rate coefficients of a few bimolecular reactions involving a Criegee intermediate as a function of the experimental activation energy. We summarized the reactions of CH_2OO with H_2O ,^{10,11} NH_3 (this work), CH_3NH_2 ,⁴ CH_3OH ,¹² $\text{C}_2\text{H}_5\text{OH}$ ¹² and H_2S ,¹³ $\text{anti-CH}_3\text{CHOO}$ with H_2O ¹⁴ and CH_3OH ,¹⁵ $\text{syn-CH}_3\text{CHOO}$ with NH_3 ,¹⁶ and $(\text{CH}_3)_2\text{COO}$ with SO_2 .¹⁷ Solid line is a linear regression to the data points except those of $\text{CH}_2\text{OO} + \text{CH}_3\text{NH}_2$ and $(\text{CH}_3)_2\text{COO} + \text{SO}_2$.

Details of Theoretical Method

The geometries in this work, including the reactants, pre-reactive complexes and the transition states, were optimized by using B3LYP^{18,19} functional with the 6-311+G(2d,2p)^{20,21} basis sets. The energies at stationary points were refined using QCISD(T)²² complete basis set (CBS) extrapolation²³ with Dunning's basis sets, aug-cc-pVDZ, aug-cc-pVTZ, aug-cc-pVQZ,²⁴⁻²⁶ at the B3LYP geometries. We extrapolated the Hartree Fock energy using $E_{\text{CBS}} + Ae^{-BX}$ while we used $E_{\text{CBS}} + Ae^{-(X-1)} + Be^{-(X-1)^2}$ to extrapolate the correlation energy, where X is the cardinal number of the basis set and E_{CBS}, A, B are optimization parameters.

All density functional theory calculations were done with the Gaussian09 program²⁷ while all QCISD(T) calculations were performed using the MOLPRO.²⁸ We performed conventional canonical transition state theory with the rigid rotor harmonic oscillator approximation using the Multiwell program²⁹ to obtain the rate coefficients. If more than one transition states are found for a product channel, the total rate coefficient is given as the sum of the contributions of all possible pathways.

Table S2. Summary of the zero-point-energy (ZPE) corrected energies of pre-reactive complex, E_{PRC} , and transition state, E_{TS} , at the level of QCISD(T)/CBS//B3LYP/6-311+G(2d,2p). The vibrational frequencies were calculated at B3LYP/6-311+G(2d,2p). The zero of energy is set to infinitely separated reactants. The calculated rate coefficients under 298 K are also listed.

QCISD(T)/CBS in kcal mol ⁻¹	Pathway	E_{PRC}	E_{TS}	Rate Coefficient
CH ₂ OO + NH ₃	1	-4.70	-0.43	1.50x10 ⁻¹³ cm ³ s ⁻¹
CH ₂ OO + 2NH ₃	2	-9.12	-8.86	1.01x10 ⁻³² cm ⁶ s ⁻¹
CH ₂ OO + H ₂ O + NH ₃ (cat.)	2a	-12.83	-7.02	8.30x10 ⁻³⁵ cm ⁶ s ⁻¹
	2b	-12.80	-7.39	1.66x10 ⁻³⁴ cm ⁶ s ⁻¹
CH ₂ OO + NH ₃ + H ₂ O(cat.)	2c	N.A. ^a	N.A. ^a	N.A. ^a

^aFor water catalysis product channel, we did not find any well-defined transition state.

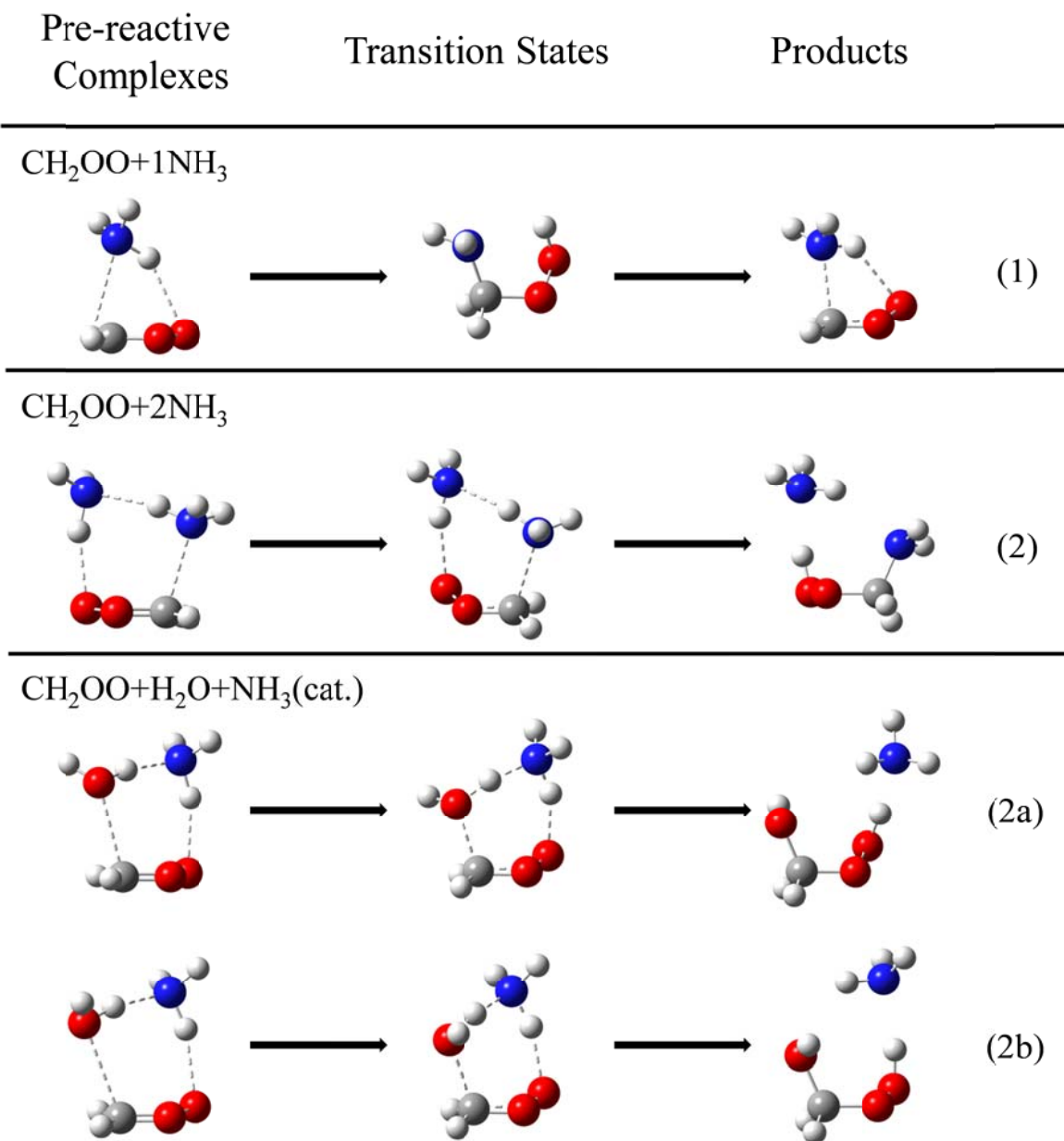


Figure S20. Pre-reactive complex, transition state and product geometries for the reactions $\text{CH}_2\text{OO} + \text{NH}_3$, $\text{CH}_2\text{OO} + 2\text{NH}_3$ and $\text{CH}_2\text{OO} + \text{H}_2\text{O} + \text{NH}_3(\text{cat.})$. For the NH_3 catalysis channel, two reaction pathways (2a, 2b), which differ by the orientation of water, were found.

Energy profiles of NH₃ catalysis channel and H₂O catalysis channel

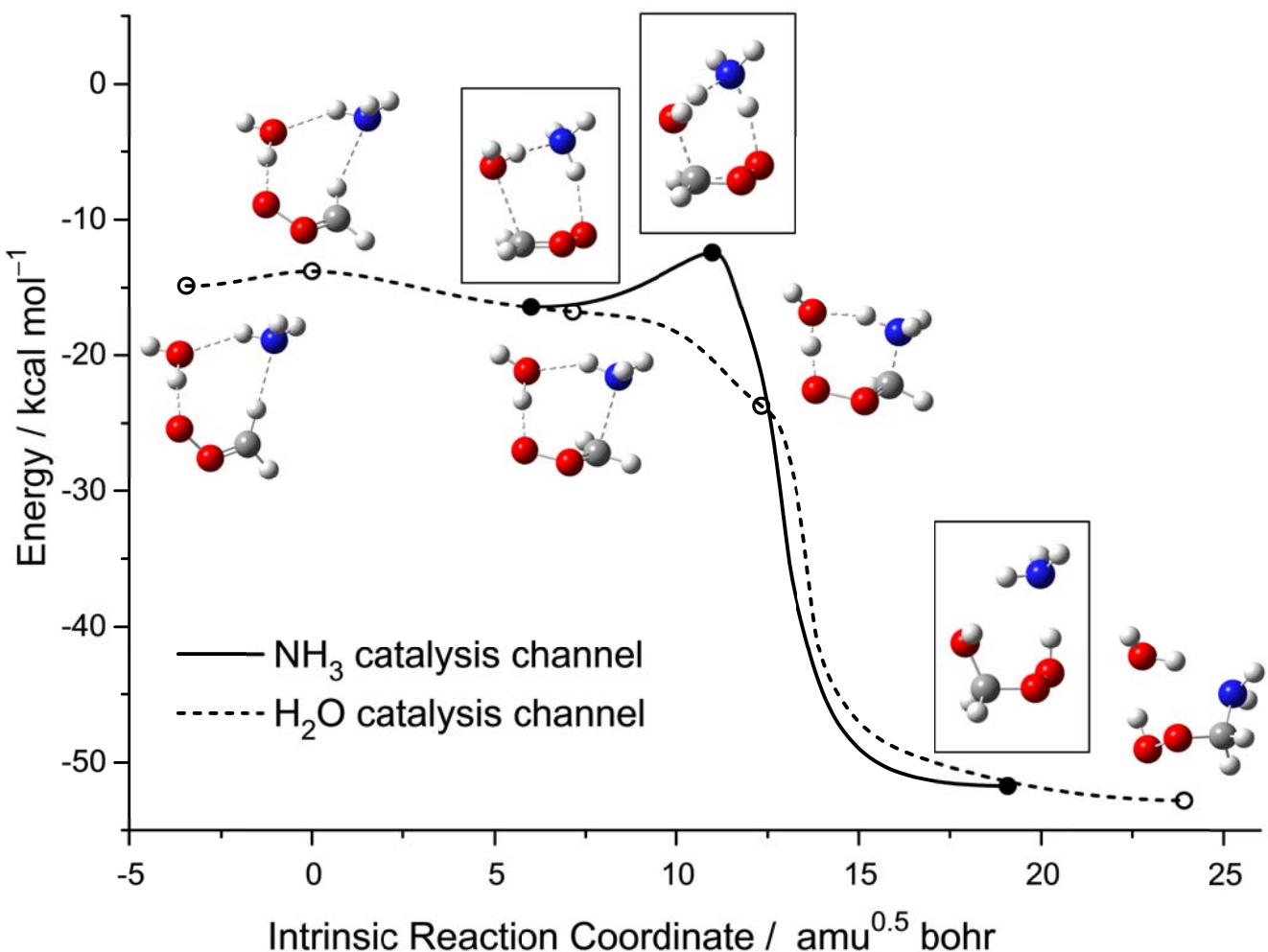


Figure S21. Plot of the calculated electronic energy (no ZPE correction) relative to the infinitely separated reactants for the NH₃ catalysis channel (path 2b, solid line) and H₂O catalysis channel (dashed line) at B3LYP/6-311+G(2d,2p) level. Representative geometries for NH₃ catalysis channel (in the box and corresponding to filled circle) and H₂O catalysis channel (corresponding to open circle) are shown.

For the H₂O catalysis channel, the reactants may form a local minimum structure of an 8-membered ring, of which NH₃ is closer to the H atom of CH₂OO rather than the carbonyl carbon atom. Along the path, we found a very low energy (less than 1 kcal mol⁻¹) saddle point for rotating NH₃ to form a 7-membered ring structure. Once the nitrogen atom approaches the carbon atom, the C–N distance decreases coupled with a drastic decrease in energy. Then the hydrogen atoms are transferred and finally a C–N bond is formed without a barrier from the 7-membered ring structure. We note that before the reaction system reaching the 7-membered ring structure, the potential energy is quite flat; it is not easy to locate TS structures for this floppy system. It is important to mention

that on the above reaction path, the imaginary vibrational frequency at the saddle point corresponds to a NH_3 rotation rather than the hydrogen transfer and nucleophilic approach to the carbonyl carbon as seen in all previous H-bonded Criegee intermediate reactions. We found that on this pathway, the NH_3 rotation from the 8-membered-ring structures to reach the elusive TS structures requires very low energies (ca. 0.6 kcal mol⁻¹). However, considering the sensitive nature of van Der Waals interactions and errors in density functional theory methods to model such weak interactions, we are not confident that the obtained saddle point is the real bottleneck for the H_2O catalysis reaction (therefore it is given as a dotted line in Figure S21). We do note that this saddle point is located ca. 4 kcal mol⁻¹ lower in energy compared to the tight 7-membered-ring TS of the NH_3 catalysis channel.

Table S3. Rotational temperature (q_R) and vibrational frequencies of the reactants, CH₂OO(H₂O) and CH₂OO(NH₃) complexes. The vibrational frequencies were calculated at B3LYP/6-311+G(2d,2p).

	H ₂ O	NH ₃	CH ₂ OO	CH ₂ OO(H ₂ O)	CH ₂ OO(NH ₃)
q_R / K	39.7231	14.3724	3.8742	0.5920	0.5111
ν / cm ⁻¹	20.6713	14.3723	0.5954	0.2059	0.2175
	13.5961	9.0446	0.5161	0.1531	0.1659
	1639.5	1036.6	531.2	60.5	76.2
	3821.4	1673.5	672.9	103.6	141.8
	3923.0	1673.6	923.4	154.3	166.7
	3482.9	948.6	207.1	204.6	
	3598.9	1247.2	458.1	237.3	
	3598.9	1402.7	551.9	404.2	
		1544.0	657.0	522.8	
		3123.8	694.4	667.6	
		3276.3	888.7	875.1	
			1020.8	976.3	
			1278.0	1081.4	
			1429.5	1243.0	
			1559.0	1415.1	
			1655.6	1567.3	
			3093.4	1665.5	
			3255.3	1688.8	
			3536.8	3139.8	
			3892.2	3287.0	
				3438.6	
				3559.8	
				3601.6	

Table S4. Summary of the energy of H-bonding complexes involving CH₂OO (E_{HC}), the partition function ($Q_{\text{HC}}/Q_{\text{R}}$) and the equilibrium constant (K_{eq}) at 298 K. The energy relative to the infinite separated reactants is calculated at QCISD(T)/CBS//B3LYP/6-311+G(2d,2p) level and zero point correction at B3LYP/6-311+G(2d,2p). The partition functions were calculated by using rigid rotor harmonic oscillator model.

$T = 298 \text{ K}$	CH ₂ OO(H ₂ O)	CH ₂ OO(NH ₃)
$E_{\text{HC}} / \text{kcal mol}^{-1}$	-6.53	-4.63
$(Q_{\text{HC}}/Q_{\text{R}}) / \text{cm}^3$	1.4×10^{-25}	9.5×10^{-26}
$K_{\text{eq}} / \text{cm}^3$	8.8×10^{-21}	2.4×10^{-22}
$k_{\text{NH}_3+\text{H}_2\text{O}} / \text{cm}^6 \text{ s}^{-1}$	$(8.2 \pm 1.2) \times 10^{-31,a}$	
$(k_{\text{NH}_3+\text{H}_2\text{O}}/K_{\text{eq}}) / \text{cm}^3 \text{ s}^{-1}$	9.3×10^{-11}	3.4×10^{-9}

^aExperimental value.

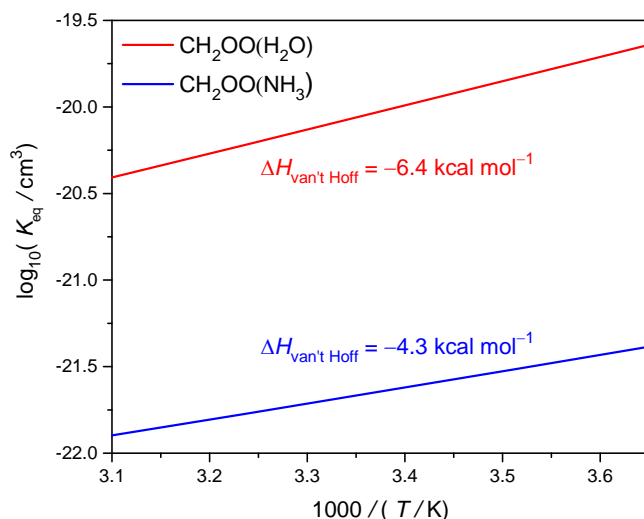


Figure S22. Van't Hoff plot of the calculated equilibrium constants of CH₂OO(H₂O) and CH₂OO(NH₃) complexes. By fitting the data to the linear form of the van't Hoff equation, $\ln(K_{\text{eq}}) = -\Delta H_{\text{van't Hoff}}/RT + \Delta S_{\text{van't Hoff}}/R$, and assuming the enthalpy and entropy changes are constant within the studied temperature range, we obtained the enthalpy change, $\Delta H_{\text{van't Hoff}}$, of the system.

Table S5. Calculated reaction rate coefficients as functions of temperature (unit: K) by using transition state theory. The unit is $\text{cm}^6 \text{ s}^{-1}$ for termolecular reactions and $\text{cm}^3 \text{ s}^{-1}$ for bimolecular reactions.

Rate Coefficient Pathway	NH_3 1	2NH_3 2	$\text{H}_2\text{O} + \text{NH}_3(\text{cat.})$		
			2a	2b	2a+2b
273.15	1.69E-13	3.99E-32	2.96E-34	6.24E-34	9.20E-34
278.15	1.65E-13	2.98E-32	2.25E-34	4.69E-34	6.94E-34
283.15	1.61E-13	2.25E-32	1.73E-34	3.57E-34	5.29E-34
288.15	1.58E-13	1.72E-32	1.34E-34	2.74E-34	4.08E-34
293.15	1.55E-13	1.33E-32	1.05E-34	2.12E-34	3.17E-34
298.15	1.52E-13	1.03E-32	8.30E-35	1.66E-34	2.49E-34
303.15	1.49E-13	8.12E-33	6.62E-35	1.31E-34	1.97E-34
308.15	1.46E-13	6.44E-33	5.32E-35	1.04E-34	1.58E-34
313.15	1.44E-13	5.15E-33	4.31E-35	8.38E-35	1.27E-34
318.15	1.42E-13	4.15E-33	3.51E-35	6.77E-35	1.03E-34
323.15	1.40E-13	3.37E-33	2.88E-35	5.52E-35	8.40E-35
328.15	1.38E-13	2.76E-33	2.38E-35	4.52E-35	6.91E-35
333.15	1.36E-13	2.28E-33	1.98E-35	3.73E-35	5.72E-35
338.15	1.35E-13	1.89E-33	1.66E-35	3.10E-35	4.76E-35
343.15	1.33E-13	1.57E-33	1.40E-35	2.59E-35	3.99E-35
348.15	1.32E-13	1.32E-33	1.18E-35	2.18E-35	3.36E-35
353.15	1.30E-13	1.12E-33	1.01E-35	1.84E-35	2.85E-35
358.15	1.29E-13	9.49E-34	8.61E-36	1.56E-35	2.42E-35
363.15	1.28E-13	8.11E-34	7.40E-36	1.33E-35	2.07E-35
368.15	1.27E-13	6.96E-34	6.39E-36	1.14E-35	1.78E-35
368.15	1.26E-13	6.00E-34	5.55E-36	9.87E-36	1.54E-35
368.15	1.25E-13	5.20E-34	4.83E-36	8.54E-36	1.34E-35

Representative Temporal Profiles

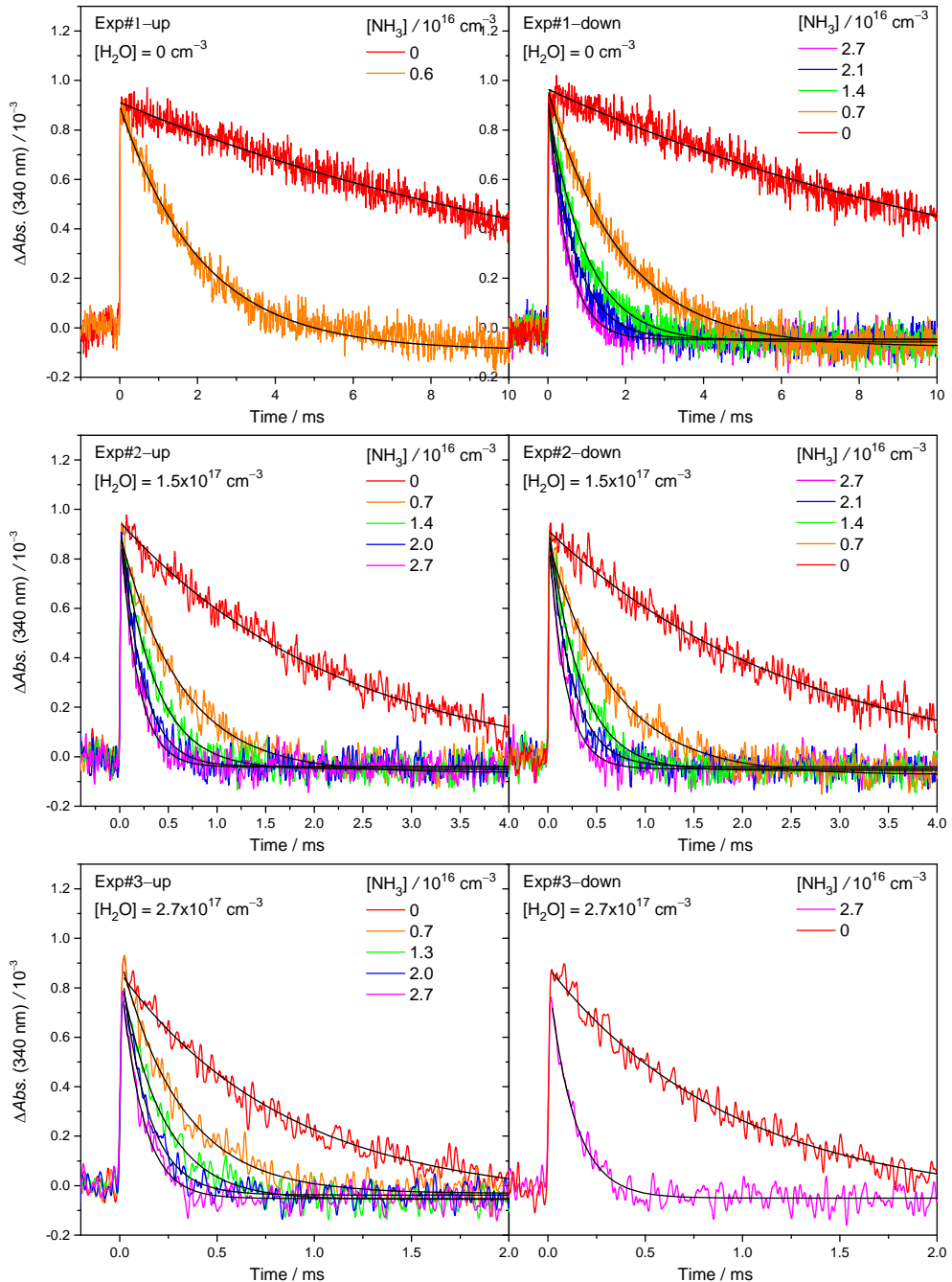


Figure S23. Temporal profiles of absorbance change of CH_2OO for exp # 1–3. For each experiment, $[\text{NH}_3]$ was scanned from 0 to the maximum (labeled as “up”) and then from the maximum to 0 (labeled as “down”). The black lines are single exponential fits to the experimental data.

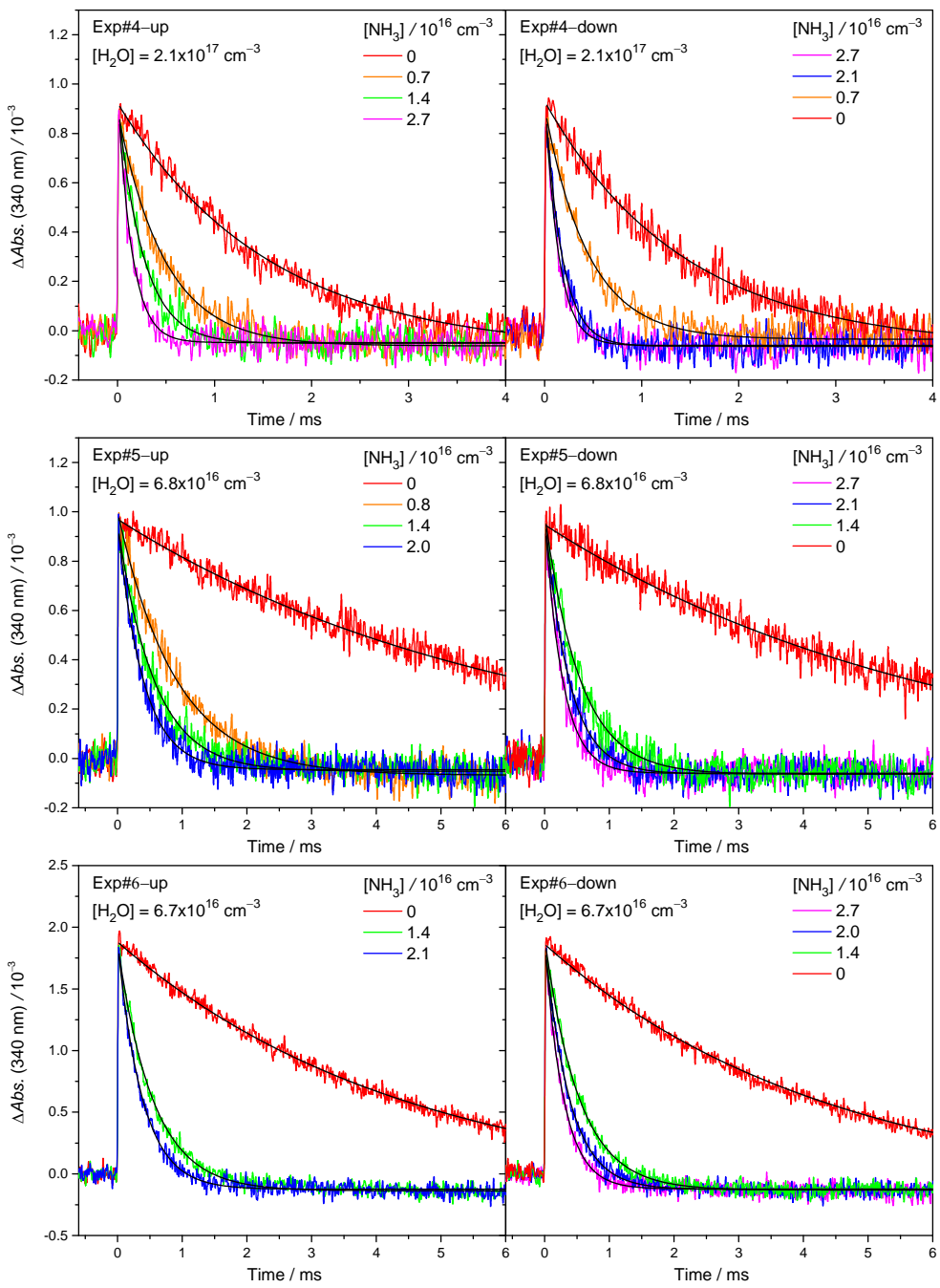


Figure S24. Temporal profiles of absorbance change of CH_2OO for exp # 4–6. For each experiment, $[\text{NH}_3]$ was scanned from 0 to the maximum (labeled as “up”) and then from the maximum to 0 (labeled as “down”). The black lines are single exponential fits to the experimental data.

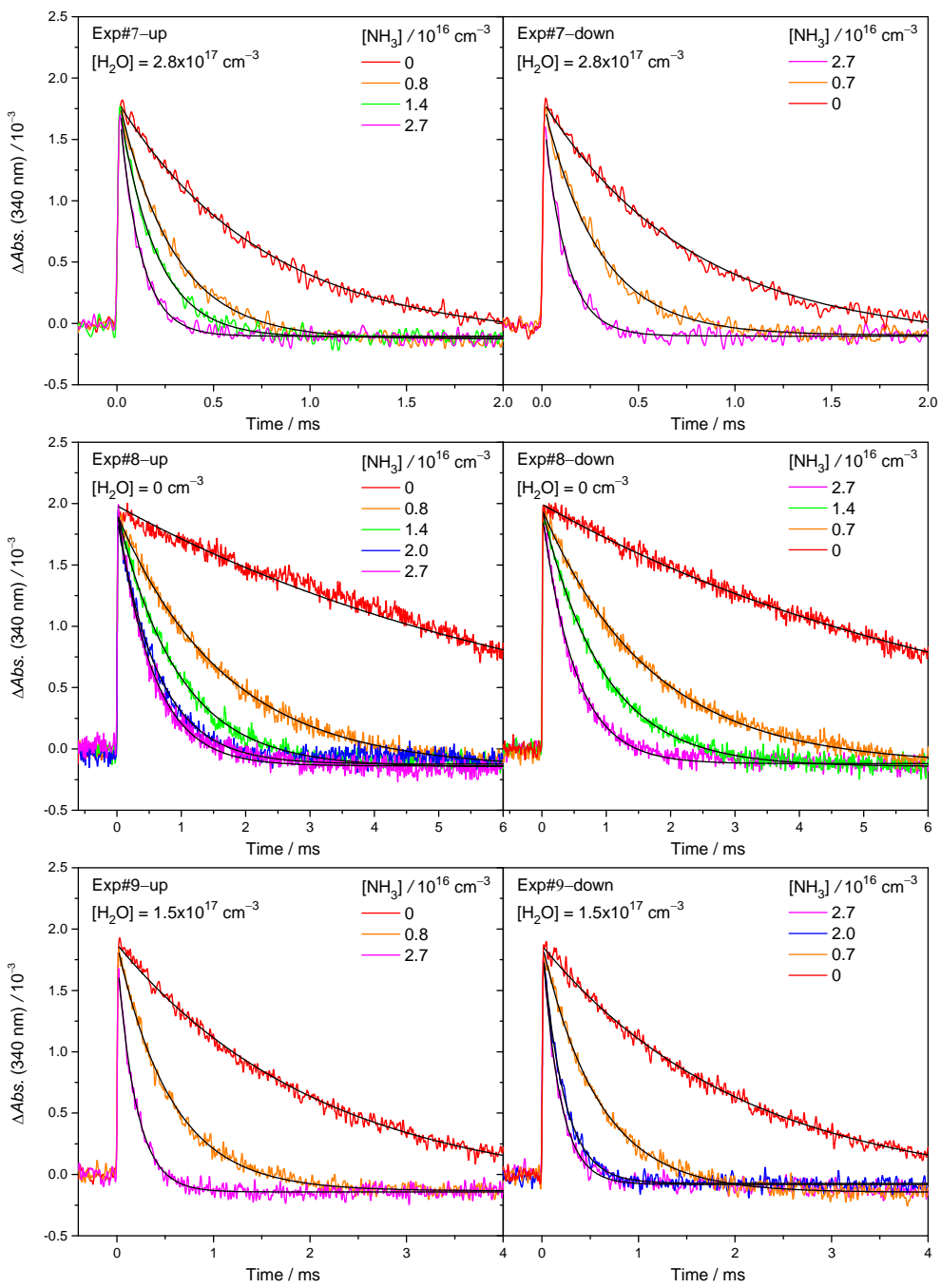


Figure S25. Temporal profiles of absorbance change of CH_2OO for exp # 7–9. For each experiment, $[\text{NH}_3]$ was scanned from 0 to the maximum (labeled as “up”) and then from the maximum to 0 (labeled as “down”). The black lines are single exponential fits to the experimental data.

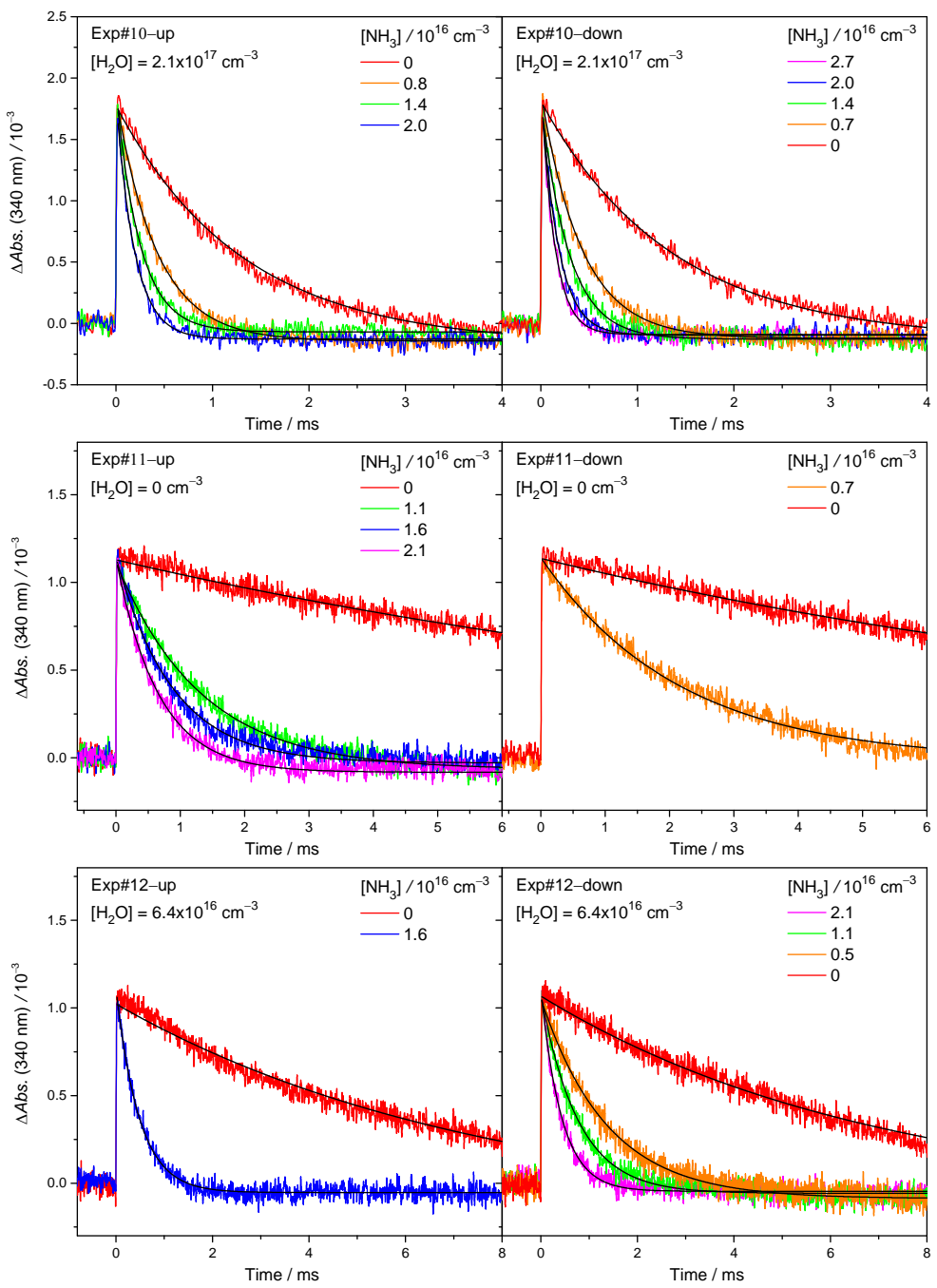


Figure S26. Temporal profiles of absorbance change of CH_2OO for exp # 10–12. For each experiment, $[\text{NH}_3]$ was scanned from 0 to the maximum (labeled as “up”) and then from the maximum to 0 (labeled as “down”). The black lines are single exponential fits to the experimental data.

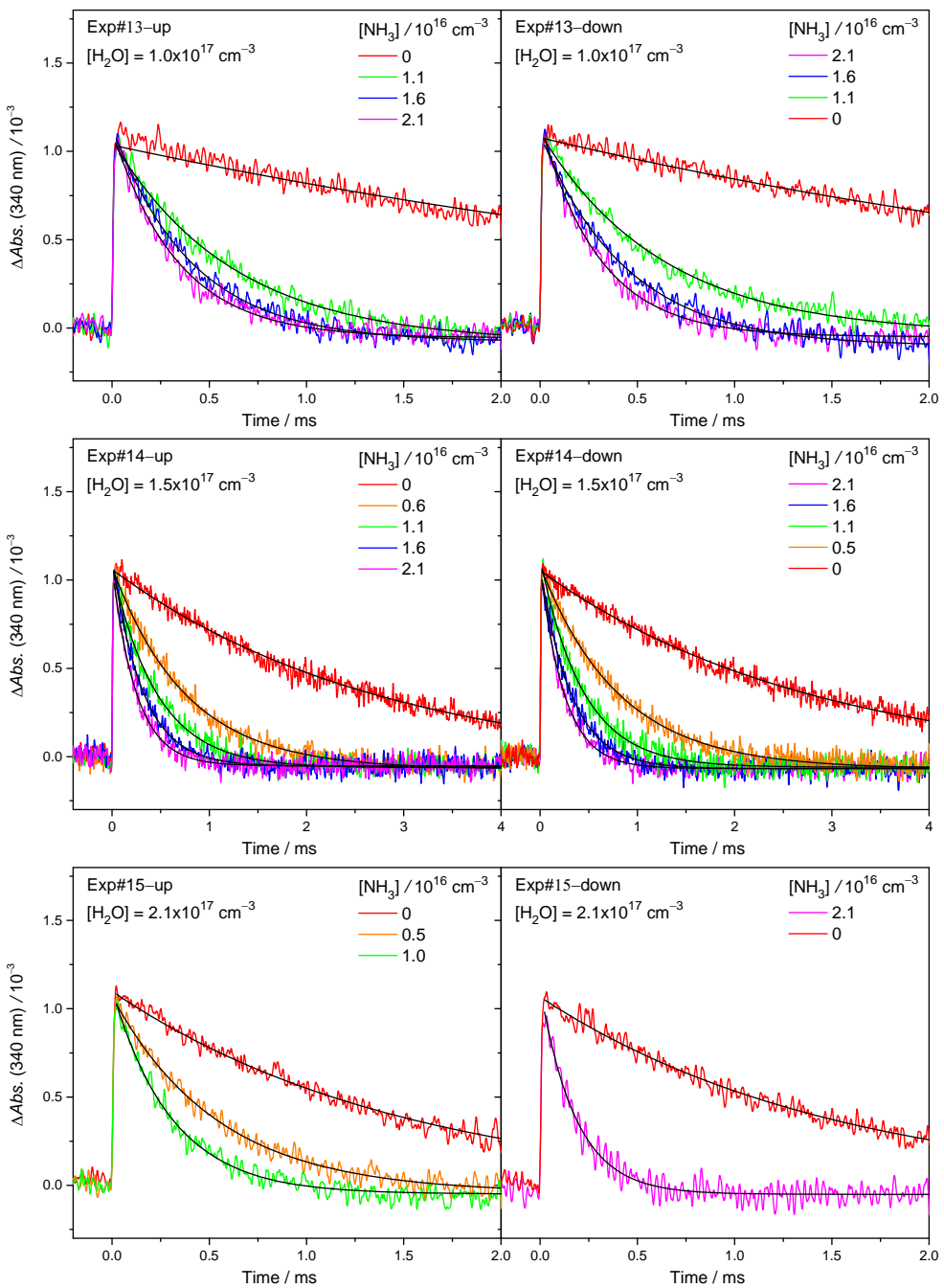


Figure S27. Temporal profiles of absorbance change of CH_2OO for exp # 13–15. For each experiment, $[\text{NH}_3]$ was scanned from 0 to the maximum (labeled as “up”) and then from the maximum to 0 (labeled as “down”). The black lines are single exponential fits to the experimental data.

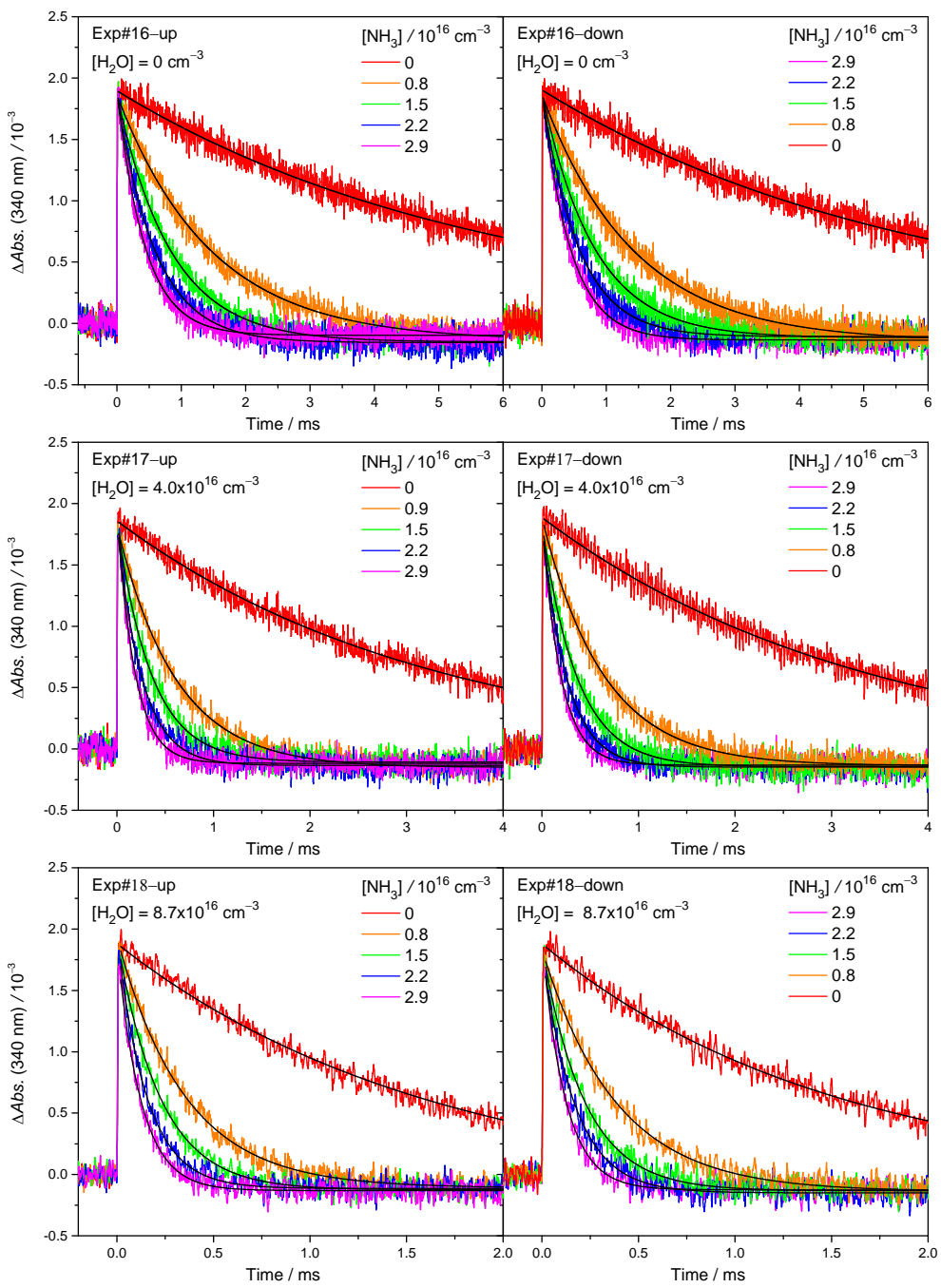


Figure S28. Temporal profiles of absorbance change of CH_2OO for exp # 16–18. For each experiment, $[NH_3]$ was scanned from 0 to the maximum (labeled as “up”) and then from the maximum to 0 (labeled as “down”). The black lines are single exponential fits to the experimental data.

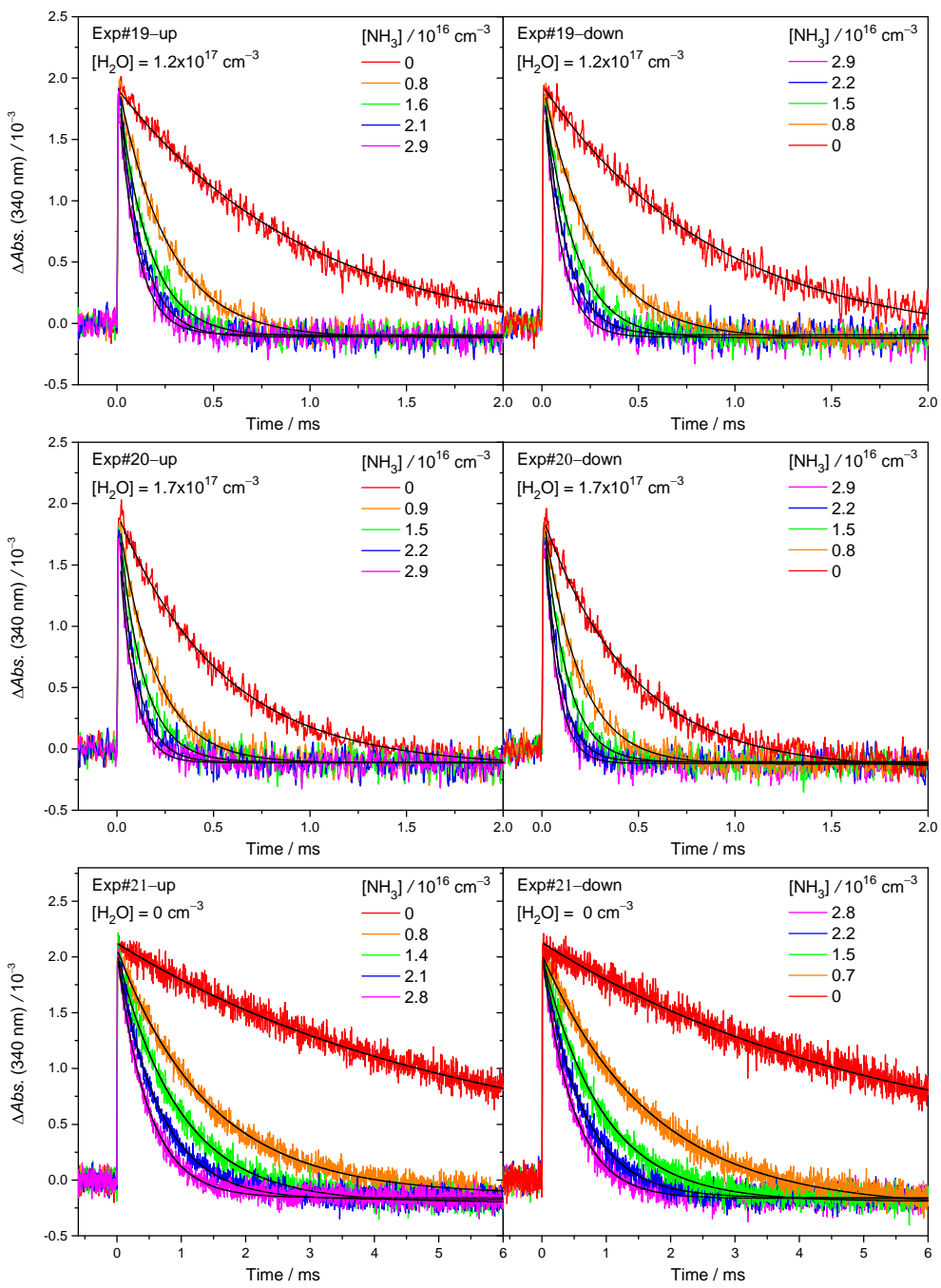


Figure S29. Temporal profiles of absorbance change of CH_2OO for exp # 19–21. For each experiment, $[\text{NH}_3]$ was scanned from 0 to the maximum (labeled as “up”) and then from the maximum to 0 (labeled as “down”). The black lines are single exponential fits to the experimental data.

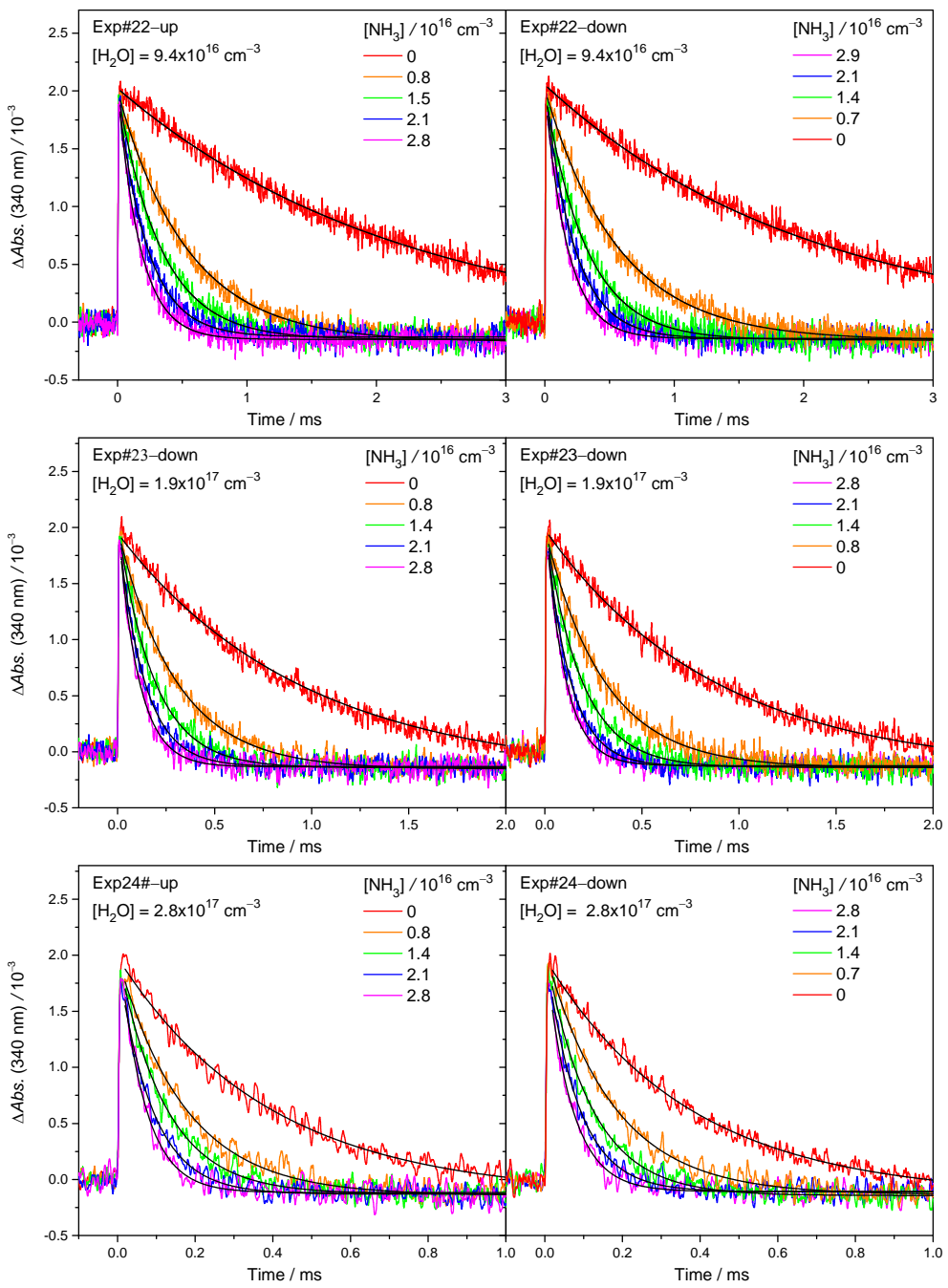


Figure S30. Temporal profiles of absorbance change of CH_2OO for exp # 22–24. For each experiment, $[\text{NH}_3]$ was scanned from 0 to the maximum (labeled as “up”) and then from the maximum to 0 (labeled as “down”). The black lines are single exponential fits to the experimental data.

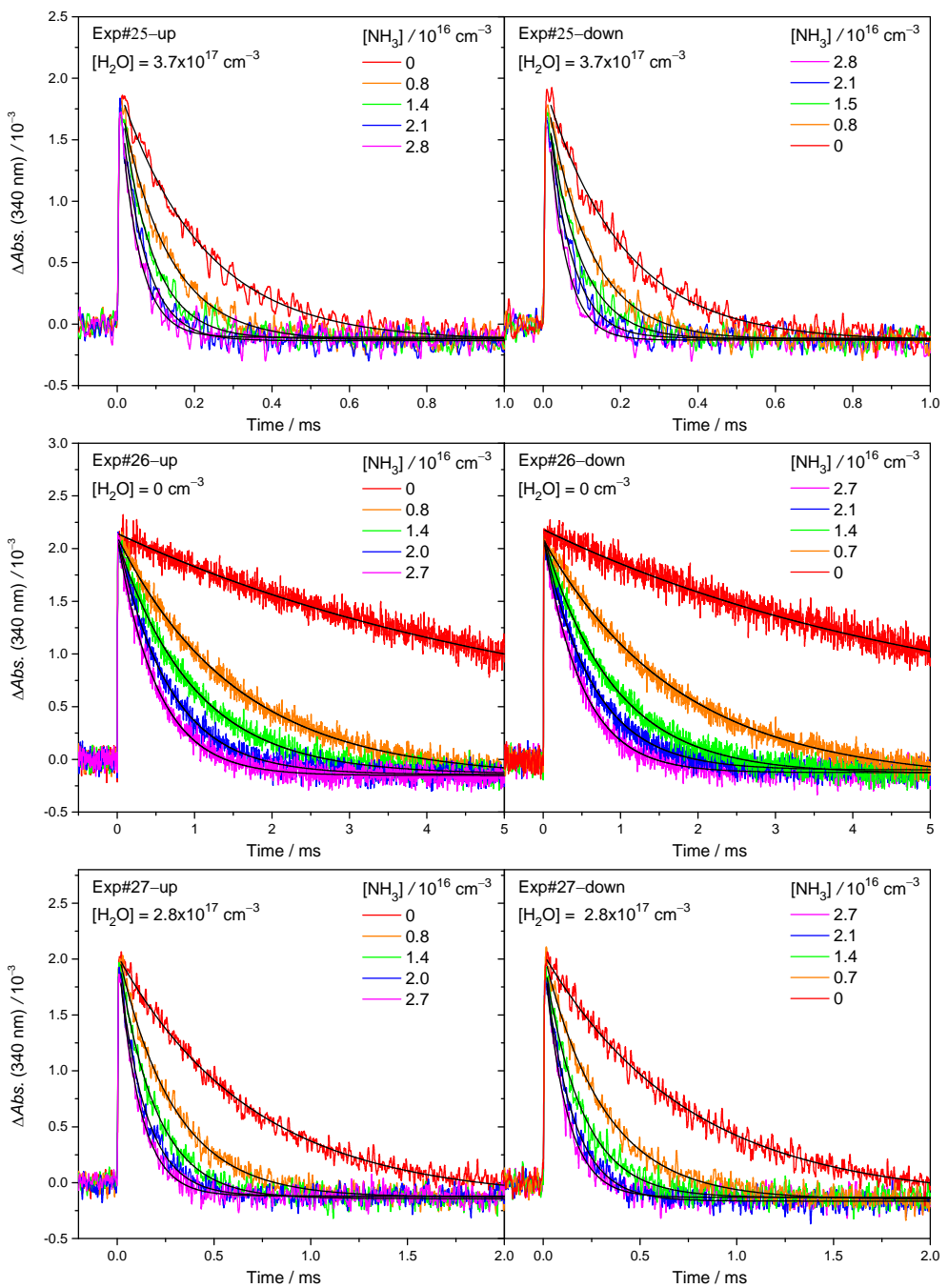


Figure S31. Temporal profiles of absorbance change of CH_2OO for exp # 25–27. For each experiment, $[\text{NH}_3]$ was scanned from 0 to the maximum (labeled as “up”) and then from the maximum to 0 (labeled as “down”). The black lines are single exponential fits to the experimental data.

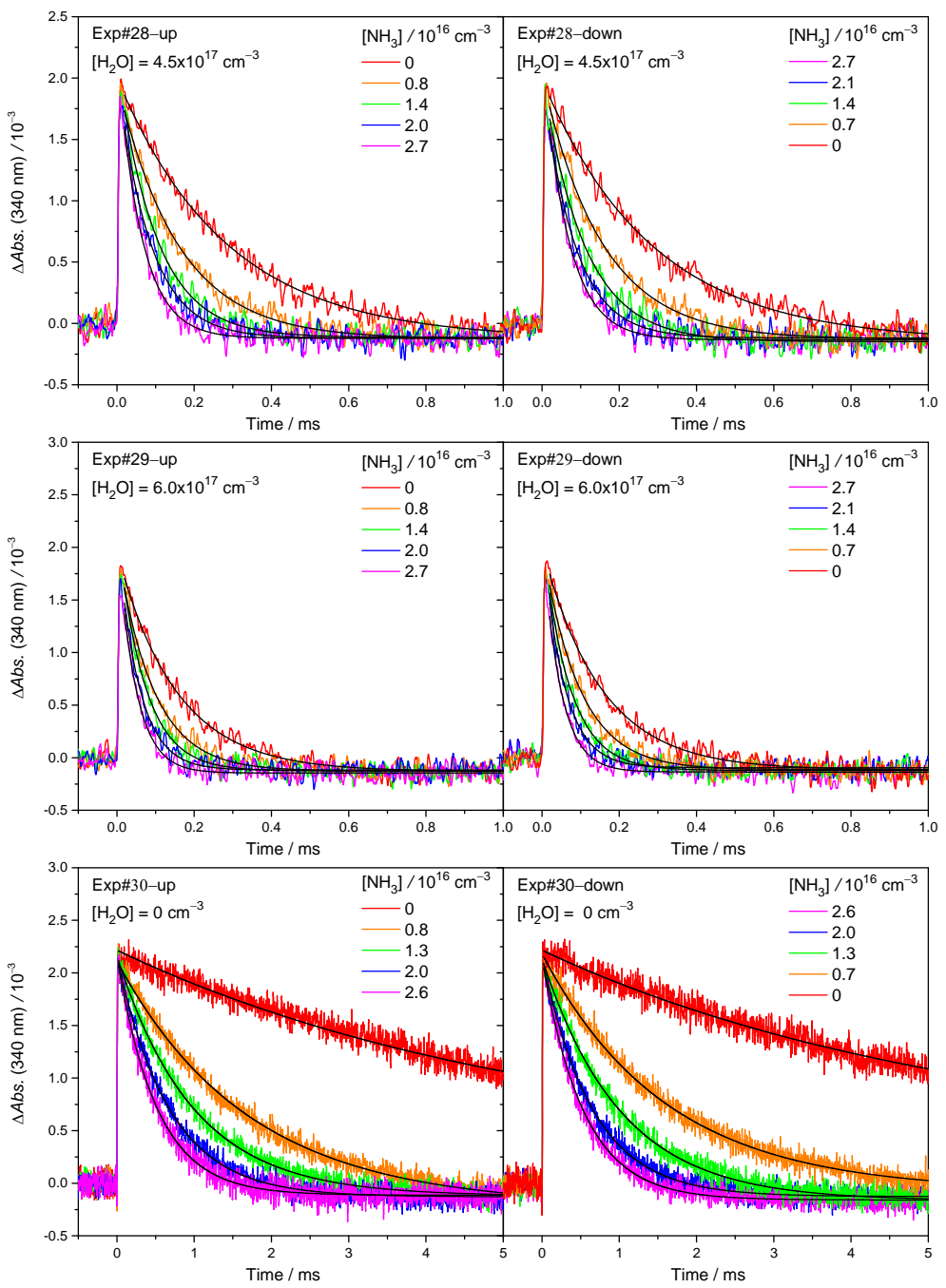


Figure S32. Temporal profiles of absorbance change of CH_2OO for exp # 28–30. For each experiment, $[\text{NH}_3]$ was scanned from 0 to the maximum (labeled as “up”) and then from the maximum to 0 (labeled as “down”). The black lines are single exponential fits to the experimental data.

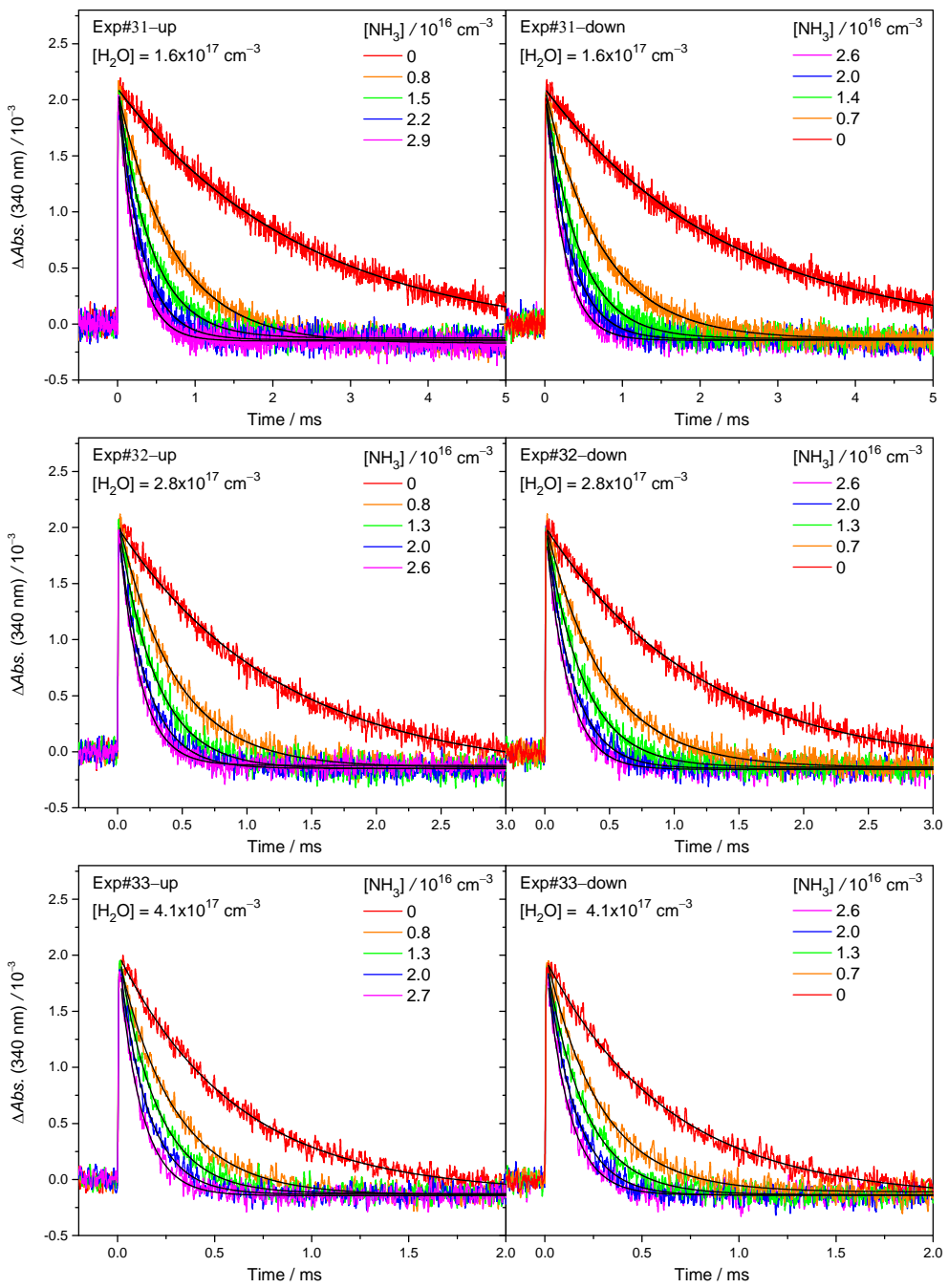


Figure S33. Temporal profiles of absorbance change of CH_2OO for exp # 31–33. For each experiment, $[\text{NH}_3]$ was scanned from 0 to the maximum (labeled as “up”) and then from the maximum to 0 (labeled as “down”). The black lines are single exponential fits to the experimental data.

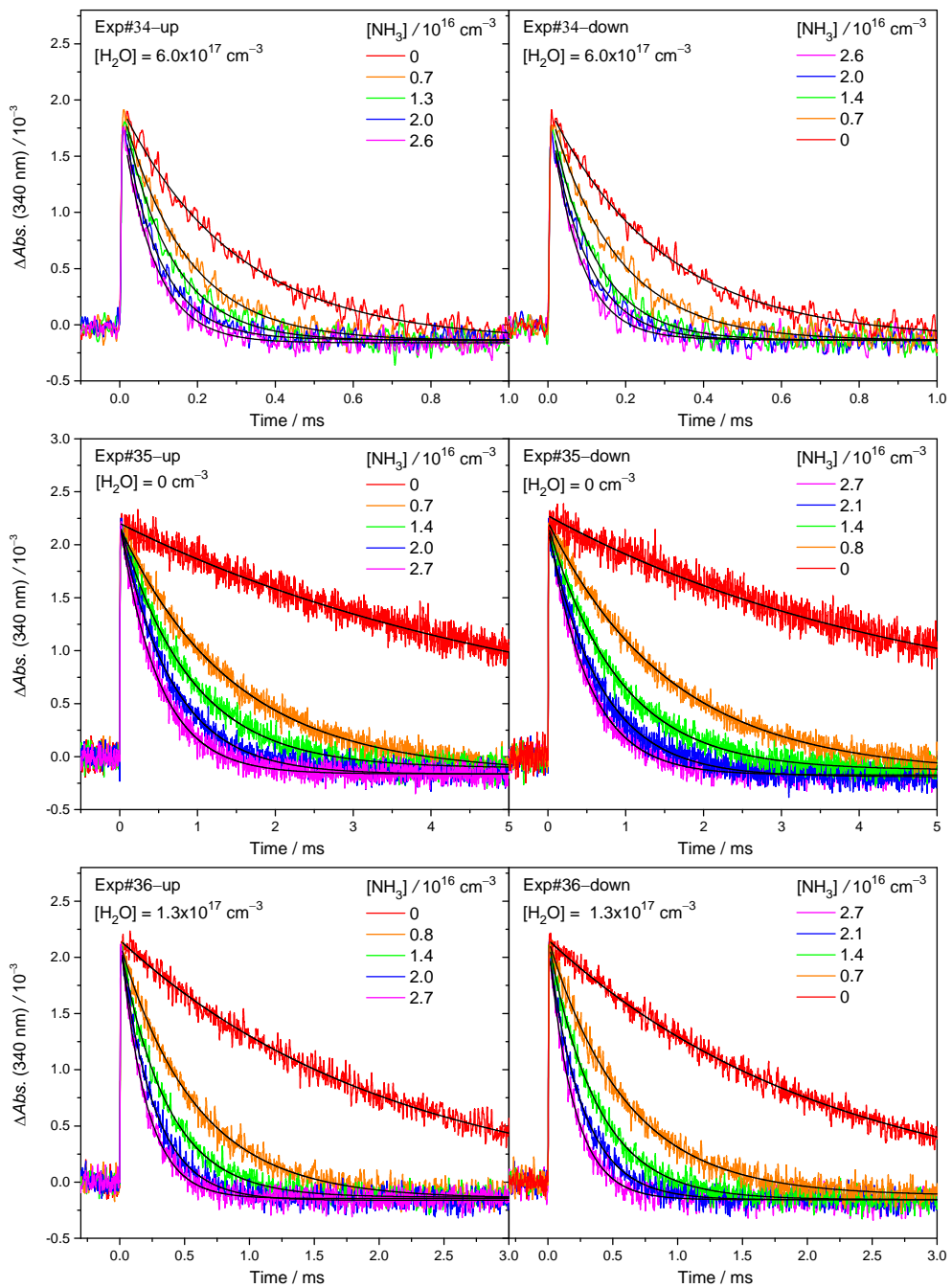


Figure S34. Temporal profiles of absorbance change of CH_2OO for exp # 34–36. For each experiment, $[\text{NH}_3]$ was scanned from 0 to the maximum (labeled as “up”) and then from the maximum to 0 (labeled as “down”). The black lines are single exponential fits to the experimental data.

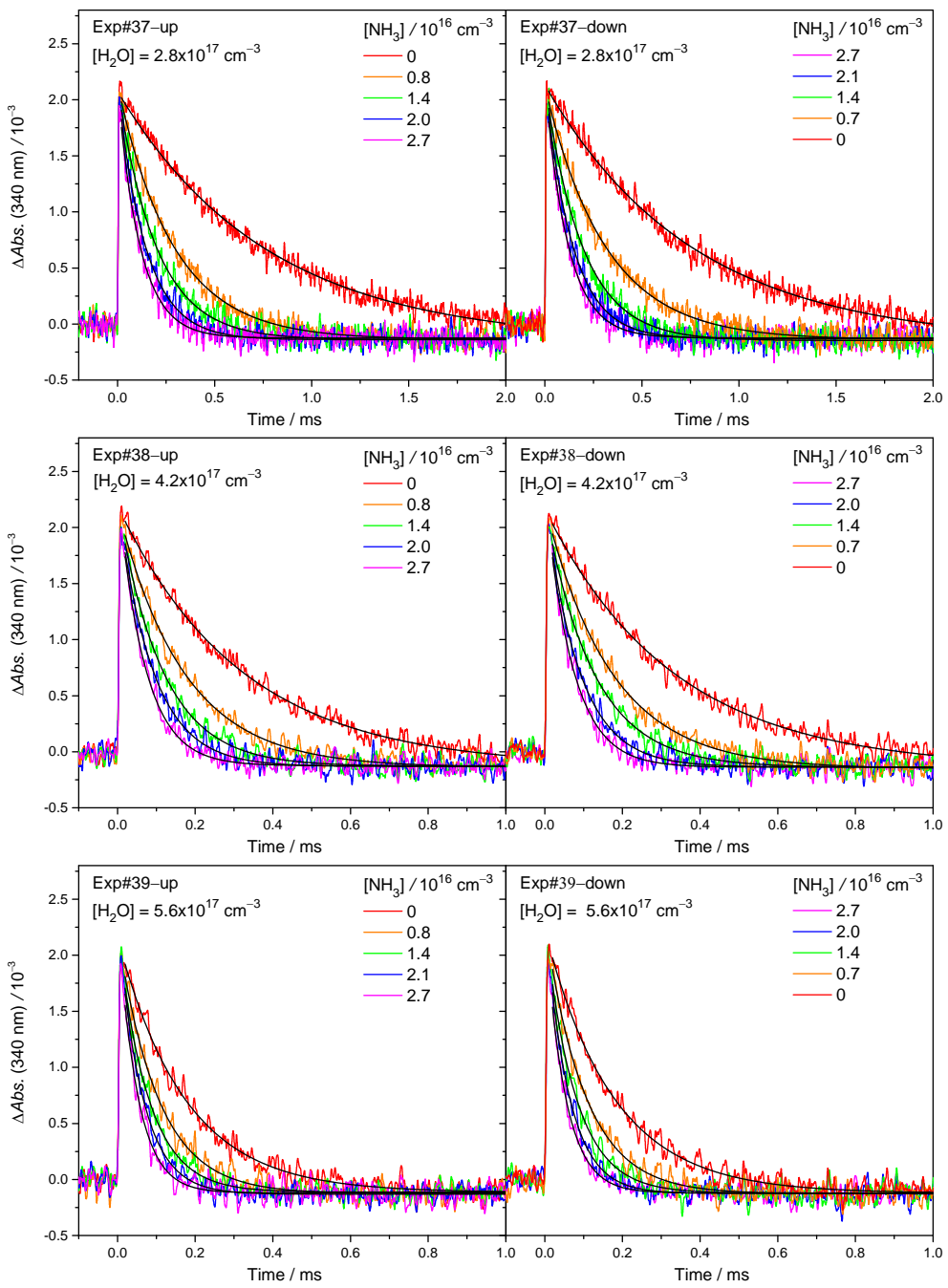


Figure S35. Temporal profiles of absorbance change of CH_2OO for exp # 37–39. For each experiment, $[\text{NH}_3]$ was scanned from 0 to the maximum (labeled as “up”) and then from the maximum to 0 (labeled as “down”). The black lines are single exponential fits to the experimental data.

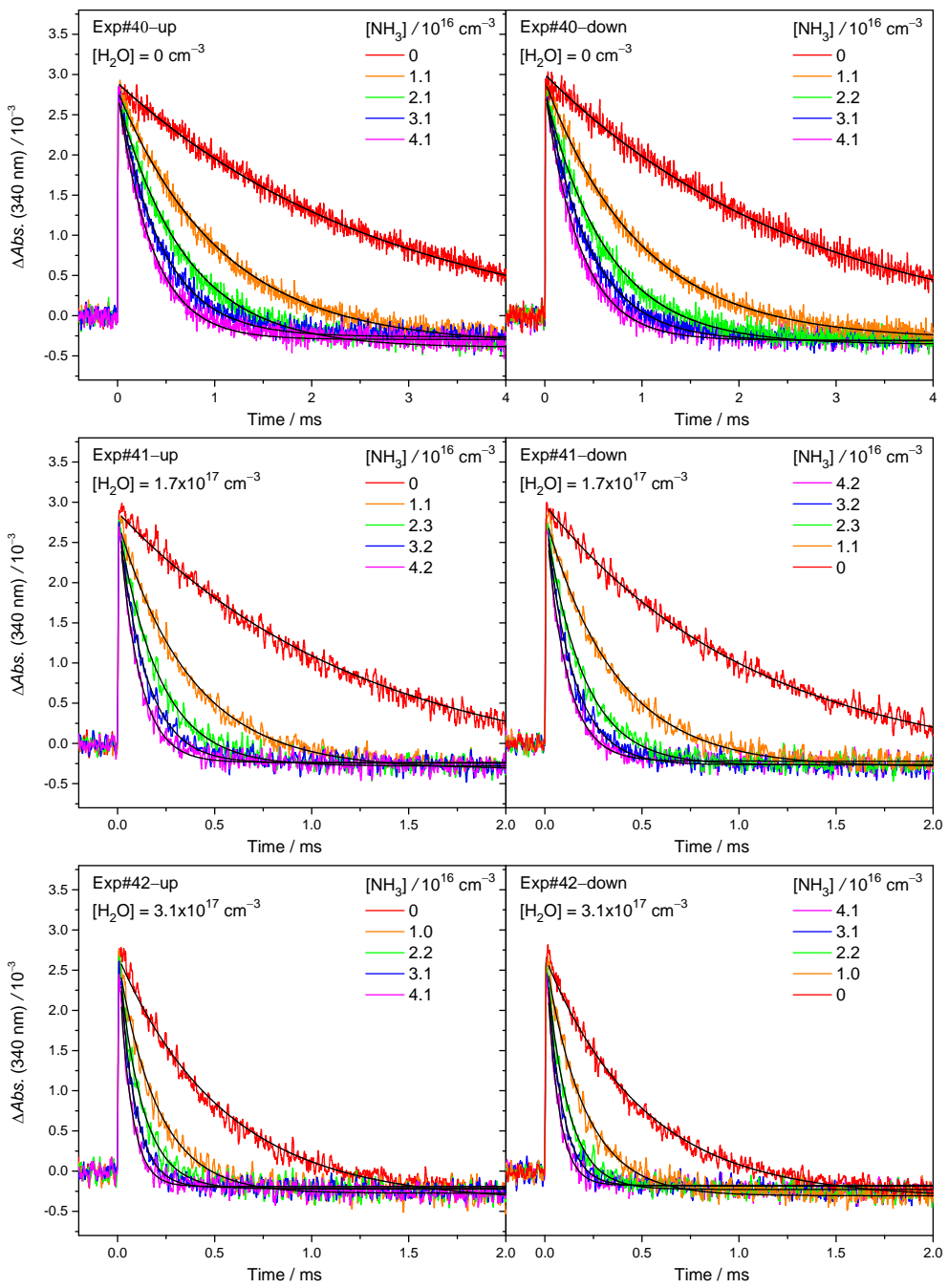


Figure S36. Temporal profiles of absorbance change of CH_2OO for exp # 40–42. For each experiment, $[\text{NH}_3]$ was scanned from 0 to the maximum (labeled as “up”) and then from the maximum to 0 (labeled as “down”). The black lines are single exponential fits to the experimental data.

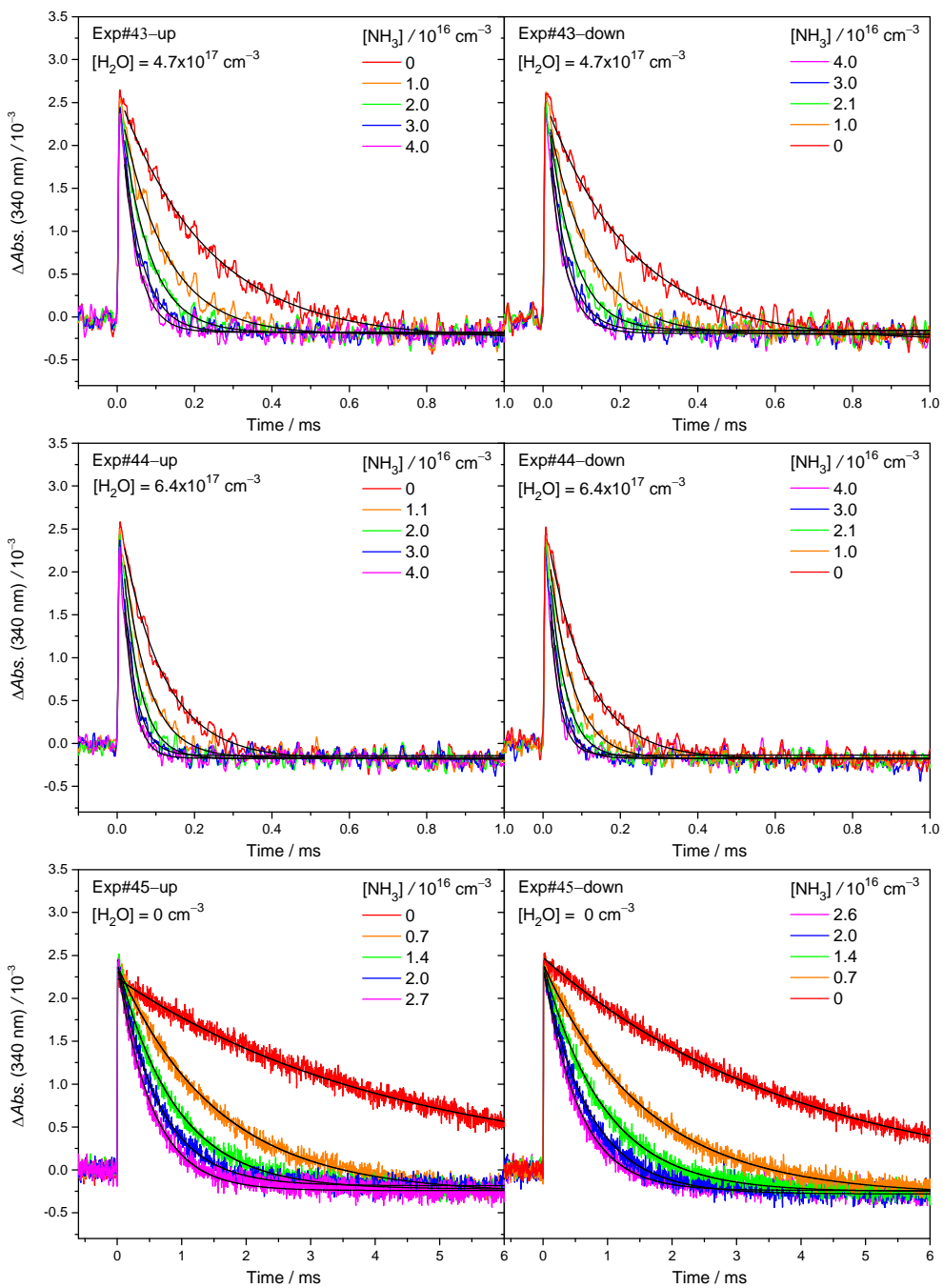


Figure S37. Temporal profiles of absorbance change of CH_2OO for exp # 43–45. For each experiment, $[\text{NH}_3]$ was scanned from 0 to the maximum (labeled as “up”) and then from the maximum to 0 (labeled as “down”). The black lines are single exponential fits to the experimental data.

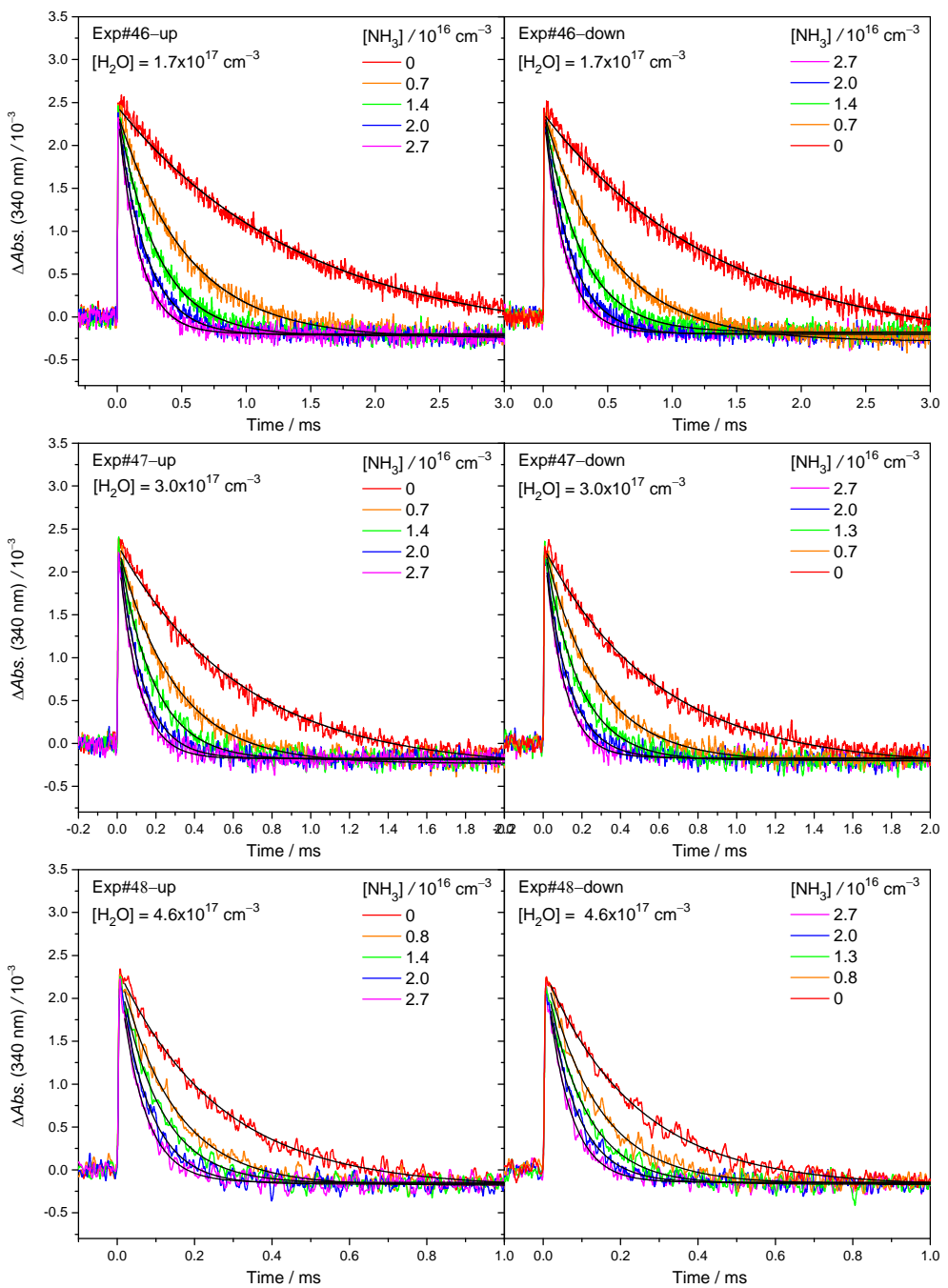


Figure S38. Temporal profiles of absorbance change of CH_2OO for exp # 46–48. For each experiment, $[\text{NH}_3]$ was scanned from 0 to the maximum (labeled as “up”) and then from the maximum to 0 (labeled as “down”). The black lines are single exponential fits to the experimental data.

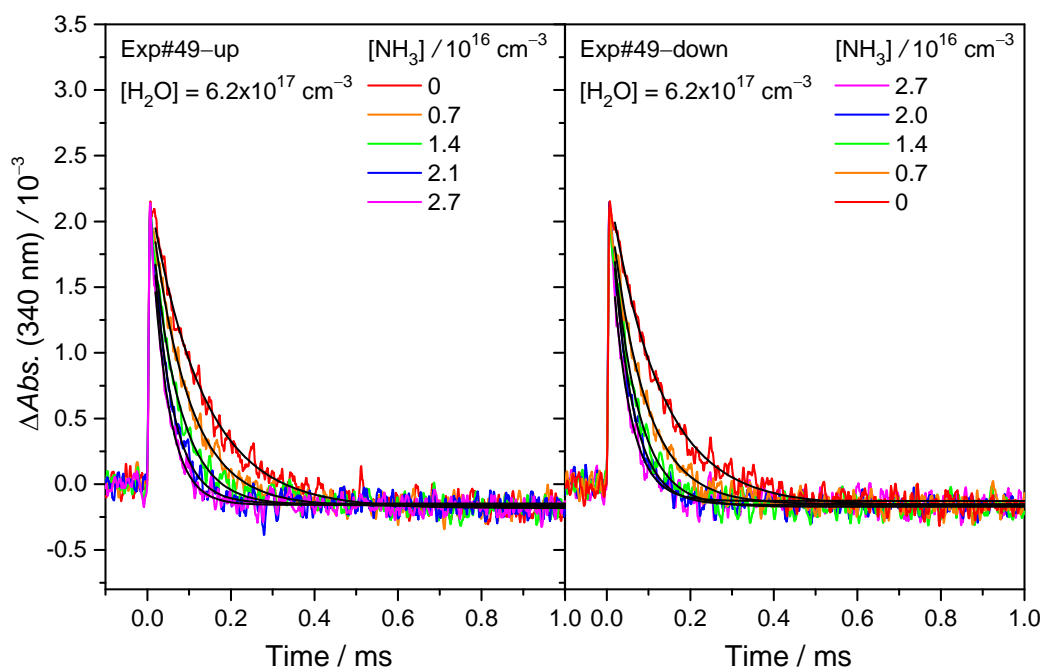


Figure S39. Temporal profiles of absorbance change of CH_2OO for exp # 49. For each experiment, $[\text{NH}_3]$ was scanned from 0 to the maximum (labeled as “up”) and then from the maximum to 0 (labeled as “down”). The black lines are single exponential fits to the experimental data.

Cartesian coordinates of the calculated geometries

Table S6. XYZ geometries (in Angström) of CH₂OO+NH₃ reaction for the pre-reactive complexes, transition states, and products, optimized at B3LYP/6-311+G(2d,2p).

CH ₂ OO+NH ₃			
Pre-reactive Complex			
	X	Y	Z
C	1.06012	-0.5865	0.36457
H	1.0833	0.18362	1.12062
H	1.9363	-1.0218	-0.096
O	-0.0331	-1.0553	-0.0177
O	-1.1801	-0.5012	0.50085
N	0.26641	1.89125	-0.753
H	-0.5918	1.43804	-0.4443
H	0.2788	2.82718	-0.3665
H	0.22422	1.9806	-1.7609
Transition State			
	X	Y	Z
C	0.97958	-0.2625	0.23839
H	0.9785	0.22853	1.20177
H	1.90648	-0.4894	-0.2759
O	-0.0129	-0.9747	-0.0898
O	-1.2118	-0.4858	0.53186
N	0.32794	1.53552	-0.6193
H	-0.6084	1.22564	-0.3217
H	0.55227	2.4397	-0.2261
H	0.38891	1.56484	-1.6282
Products			
	X	Y	Z
C	0.91403	0.08987	0.09032
H	1.04933	0.26773	1.15784
H	1.81668	-0.3613	-0.3296
O	-0.0498	-0.9342	-0.1037
O	-1.2645	-0.5187	0.56399
N	0.50694	1.31663	-0.5539
H	-1.5224	0.2384	0.01314
H	0.74434	2.14229	-0.0257
H	0.84535	1.40638	-1.5007

Table S7. XYZ geometries (in Angström) of CH₂OO+2NH₃ reaction for the pre-reactive complexes, transition states, and products, optimized at B3LYP/6-311+G(2d,2p).

CH ₂ OO+2NH ₃			
Pre-reactive Complex			
	X	Y	Z
C	-0.9649	-0.0698	-0.5907
O	0.83609	1.27292	-0.793
O	-0.4303	1.00281	-0.2263
N	-0.0913	-1.7539	0.79734
N	2.52698	-0.2534	1.09064
H	0.01677	-2.6859	0.41399
H	0.8438	-1.3666	0.99167
H	-0.5936	-1.8355	1.67353
H	2.79384	0.25028	1.92837
H	3.3839	-0.5826	0.66165
H	2.0949	0.41911	0.44587
H	-0.5339	-0.6219	-1.4126
H	-1.9602	-0.2492	-0.211
Transition State			
	X	Y	Z
C	-1.0302	0.04346	-0.6822
O	0.79068	1.35352	-0.9194
O	-0.4838	1.11894	-0.3323
N	-0.1917	-1.5684	0.64075
N	2.43205	-0.1539	0.98052
H	-0.1057	-2.4947	0.23848
H	0.7525	-1.2019	0.84554
H	-0.7053	-1.6492	1.51039
H	2.69273	0.34934	1.8204
H	3.29039	-0.4986	0.56692
H	2.01726	0.52132	0.32429
H	-0.6317	-0.493	-1.531
H	-2.0346	-0.109	-0.3132
Products			
	X	Y	Z
C	-0.914	-0.4133	-0.5659
O	1.01972	0.73393	-1.1122
O	-0.2493	0.82568	-0.415

N	-0.3694	-1.4721	0.26882
N	2.37102	0.00974	1.23567
H	-0.069	-2.273	-0.2668
H	1.58489	-0.6267	1.34551
H	-1.0164	-1.7781	0.98047
H	2.34325	0.68465	1.98981
H	3.23088	-0.5177	1.31855
H	1.63305	0.56467	-0.3544
H	-0.8839	-0.696	-1.6182
H	-1.9391	-0.1714	-0.2799

Table S8. XYZ geometries (in Angström) of CH₂OO+H₂O+NH₃(cat.) reaction for the pre-reactive complexes, transition states, and products, optimized at B3LYP/6-311+G(2d,2p).

CH ₂ OO+H ₂ O+NH ₃ (cat), 2a			CH ₂ OO+H ₂ O+NH ₃ (cat), 2b				
Pre-reactive Complex			Pre-reactive Complex				
X	Y	Z	X	Y	Z		
C	1.5078	0.049	-0.4404	C	1.45173	0.06751	-0.4639
O	0.75105	-0.885	-0.7676	O	0.78403	-0.9163	-0.8379
O	0.22518	-1.6701	0.25189	O	0.17771	-1.6917	0.14367
O	-0.0762	2.03533	-0.0071	O	-0.0938	2.06173	0.01194
H	-0.845	1.49123	0.30733	H	-0.8435	1.51196	0.36229
H	-0.0186	2.78547	0.58987	H	-0.4737	2.63081	-0.6621
N	-2.0408	0.20648	0.77466	N	-1.9393	0.22162	1.00366
H	-1.437	-0.6128	0.65996	H	-1.3579	-0.5943	0.78913
H	-2.832	0.09883	0.15095	H	-2.8439	0.07911	0.57052
H	-2.4019	0.19435	1.72107	H	-2.0873	0.24477	2.00563
H	1.7643	0.18966	0.60007	H	1.58267	0.26369	0.59055
H	1.88901	0.65012	-1.2525	H	1.90893	0.6499	-1.2502
Transition State			Transition State				
X	Y	Z	X	Y	Z		
C	1.27793	0.2783	-0.4658	C	1.26806	0.28703	-0.3628
O	0.60047	-0.756	-0.7647	O	0.68659	-0.7384	-0.8442
O	0.21041	-1.5097	0.4205	O	0.0992	-1.5781	0.19039
O	0.0738	1.65187	0.00637	O	0.03403	1.66731	-0.0376
H	-0.8585	1.08793	0.3103	H	-0.8448	1.12015	0.40501
H	0.406	2.1035	0.79029	H	-0.2371	1.99104	-0.904
N	-1.8791	0.17824	0.61924	N	-1.7747	0.20869	0.93965
H	-1.2576	-0.6756	0.61455	H	-1.205	-0.653	0.71026
H	-2.5971	0.0893	-0.0892	H	-2.6812	0.1573	0.49173
H	-2.3308	0.27194	1.52031	H	-1.9171	0.27217	1.94003
H	1.80674	0.27148	0.47949	H	1.57349	0.25732	0.67475
H	1.6832	0.80368	-1.3209	H	1.86023	0.84087	-1.0816
Products			Products				
X	Y	Z	X	Y	Z		
C	1.28419	0.44858	-0.6019	C	1.27928	0.46015	-0.4806
O	0.4571	-0.6712	-0.7719	O	0.58806	-0.6874	-0.8794
O	0.23164	-1.2332	0.54992	O	0.15069	-1.4021	0.30418
O	0.64455	1.53392	0.02873	O	0.43578	1.53947	-0.1133

H	-2.0091	0.75205	0.14359	H	-1.6414	0.91169	1.02756
H	0.65622	1.36802	0.97609	H	0.02289	1.8788	-0.9134
N	-2.324	-0.0854	0.62256	N	-2.15	0.03375	1.04828
H	-0.7034	-0.94	0.6976	H	-0.724	-0.9791	0.49788
H	-2.9601	-0.571	0.00117	H	-2.9582	0.12071	0.44443
H	-2.8507	0.19945	1.43935	H	-2.4844	-0.1162	1.99237
H	2.18419	0.15866	-0.0557	H	1.89806	0.24673	0.38712
H	1.52275	0.75738	-1.6184	H	1.88692	0.71981	-1.3509

References

- 1 B. Cheng, H. Lu, H. Chen, M. Bahou, Y. Lee, A. M. Mebel, L. C. Lee, M. Liang and Y. L. Yung, *Astrophys. J.*, 2006, **647**, 1535–1542.
- 2 W. L. Ting, Y. H. Chen, W. Chao, M. C. Smith and J. J. Lin, *Phys. Chem. Chem. Phys.*, 2014, **16**, 10438–10443.
- 3 Y. Liu, C. Yin, M. C. Smith, S. Liu, M. Chen, X. Zhou, C. Xiao, D. Dai, J. J. Lin, K. Takahashi, W. Dong and X. Yang, *Phys. Chem. Chem. Phys.*, 2018, **20**, 29669–29676.
- 4 R. Chhantyal-Pun, R. J. Shannon, D. P. Tew, R. L. Caravan, M. Duchi, C. Wong, A. Ingham, C. Feldman, M. R. McGillen, M. A. H. Khan, I. O. Antonov, B. Rotavera, K. Ramasesha, D. L. Osborn, C. A. Taatjes, C. J. Percival, D. E. Shallcross and A. J. Orr-Ewing, *Phys. Chem. Chem. Phys.*, 2019, **21**, 14042–14052.
- 5 M. C. Smith, C. H. Chang, W. Chao, L. C. Lin, K. Takahashi, K. A. Boering and J. J. Lin, *J. Phys. Chem. Lett.*, 2015, **6**, 2708–2713.
- 6 T. Berndt, J. Voigtländer, F. Stratmann, H. Junninen, R. L. Mauldin, M. Sipilä, M. Kulmala and H. Herrmann, *Phys. Chem. Chem. Phys.*, 2014, **16**, 19130–19136.
- 7 H.-L. Huang, W. Chao and J. J. Lin, *Proc. Natl. Acad. Sci.*, 2015, **112**, 10857–10862.
- 8 L. Sheps, B. Rotavera, A. J. Eskola, D. L. Osborn, C. A. Taatjes, K. Au, D. E. Shallcross, M. A. H. Khan and C. J. Percival, *Phys. Chem. Chem. Phys.*, 2017, **19**, 21970–21979.
- 9 T. R. Lewis, M. A. Blitz, D. E. Heard and P. W. Seakins, *Phys. Chem. Chem. Phys.*, 2015, **17**, 4859–4863.
- 10 L. C. Lin, H. T. Chang, C. H. Chang, W. Chao, M. C. Smith, C. H. Chang, J. J. Lin and K. Takahashi, *Phys. Chem. Chem. Phys.*, 2016, **18**, 4557–4568.
- 11 T. Berndt, R. Kaethner, J. Voigtländer, F. Stratmann, M. Pfeifle, P. Reichle, M. Sipilä, M. Kulmala and M. Olzmann, *Phys. Chem. Chem. Phys.*, 2015, **17**, 19862–19873.
- 12 M. R. McGillen, B. F. E. Curchod, R. Chhantyal-Pun, J. M. Beames, N. Watson, M. A. H. Khan, L. McMahon, D. E. Shallcross and A. J. Orr-Ewing, *ACS Earth Sp. Chem.*, 2017, **1**, 664–672.
- 13 M. C. Smith, W. Chao, M. Kumar, J. S. Francisco, K. Takahashi and J. J. Lin, *J. Phys. Chem. A*, 2017, **121**, 938–945.
- 14 L.-C. Lin, W. Chao, C.-H. Chang, K. Takahashi and J. J. Lin, *Phys. Chem. Chem. Phys.*, 2016, **18**, 28189–28197.
- 15 W. Chao, Y.-H. Lin, C. Yin, W.-H. Lin, K. Takahashi and J. J. Lin, *Phys. Chem. Chem. Phys.*, 2019, **21**, 13633–13640.
- 16 W. Chao, C. Yin, Y. L. Li, K. Takahashi and J. J. Lin, *J. Phys. Chem. A*, 2019, **123**, 1337–1342.
- 17 M. C. Smith, W. Chao, K. Takahashi, K. A. Boering and J. J. Lin, *J. Phys. Chem. A*, 2016, **120**, 4789–4798.
- 18 A. D. Becke, *J. Chem. Phys.*, 1993, **98**, 5648–5652.

- 19 C. Lee, W. Yang and R. G. Parr, *Phys. Rev. B*, 1988, **37**, 785–789.
- 20 R. Krishnan, J. S. Binkley, R. Seeger and J. A. Pople, *J. Chem. Phys.*, 1980, **72**, 650–654.
- 21 M. J. Frisch, J. A. Pople and J. S. Binkley, *J. Chem. Phys.*, 1984, **80**, 3265–3269.
- 22 J. A. Pople, M. Head-Gordon and K. Raghavachari, *J. Chem. Phys.*, 1987, **87**, 5968–5975.
- 23 K. A. Peterson, D. E. Woon and T. H. Dunning, *J. Chem. Phys.*, 1994, **100**, 7410–7415.
- 24 T. H. Dunning, *J. Chem. Phys.*, 1989, **90**, 1007–1023.
- 25 R. A. Kendall, T. H. Dunning and R. J. Harrison, *J. Chem. Phys.*, 1992, **96**, 6796–6806.
- 26 J. Dunning, K. A. Peterson and A. K. Wilson, *J. Chem. Phys.*, 2001, **114**, 9244–9253.
- 27 M. J. Frisch *et al.*, Gaussian, Inc., Wallingford, CT, 2009.
- 28 H. J. Werner and P. J. Knowles, 1999.
- 29 J. R. Barker, T. L. Nguyen, J. F. Stanton, C. Aieta, M. Ceotto, F. Gabas, T. J. D. Kumar, C. G. L. Li, L. L. Lohr, A. Maranzana, N. F. Ortiz, J. M. Preses and P. J. Stimac, UNIVERSITY OF MICHIGAN, 2016.